



**HAL**  
open science

# CH<sub>3</sub>OH and Its Deuterated Species in the Disk/Envelope System of the Low-mass Protostellar Source B335

Yuki Okoda, Yoko Oya, Nami Sakai, Yoshimasa Watanabe, Ana López-Sepulcre, Takahiro Oyama, Shaoshan Zeng, Satoshi Yamamoto

► **To cite this version:**

Yuki Okoda, Yoko Oya, Nami Sakai, Yoshimasa Watanabe, Ana López-Sepulcre, et al.. CH<sub>3</sub>OH and Its Deuterated Species in the Disk/Envelope System of the Low-mass Protostellar Source B335. *The Astrophysical Journal*, 2024, 970, 10.3847/1538-4357/ad4d88 . insu-04836846

**HAL Id: insu-04836846**

**<https://insu.hal.science/insu-04836846v1>**

Submitted on 14 Dec 2024

**HAL** is a multi-disciplinary open access archive for the deposit and dissemination of scientific research documents, whether they are published or not. The documents may come from teaching and research institutions in France or abroad, or from public or private research centers.

L'archive ouverte pluridisciplinaire **HAL**, est destinée au dépôt et à la diffusion de documents scientifiques de niveau recherche, publiés ou non, émanant des établissements d'enseignement et de recherche français ou étrangers, des laboratoires publics ou privés.



Distributed under a Creative Commons Attribution 4.0 International License



# CH<sub>3</sub>OH and Its Deuterated Species in the Disk/Envelope System of the Low-mass Protostellar Source B335

Yuki Okoda<sup>1</sup> , Yoko Oya<sup>2,3</sup>, Nami Sakai<sup>1</sup> , Yoshimasa Watanabe<sup>4</sup> , Ana López-Sepulcre<sup>5,6</sup> , Takahiro Oyama<sup>1</sup> ,  
Shaoshan Zeng<sup>1</sup> , and Satoshi Yamamoto<sup>7,8</sup>

<sup>1</sup>RIKEN Cluster for Pioneering Research, 2-1, Hirosawa, Wako-shi, Saitama 351-0198, Japan; [yuki.okoda@riken.jp](mailto:yuki.okoda@riken.jp)

<sup>2</sup>Center for Gravitational Physics and Quantum Information, Yukawa Institute for Theoretical Physics, Kyoto University, Kyoto, 606-8502, Japan

<sup>3</sup>Department of Physics, The University of Tokyo, 7-3-1, Hongo, Bunkyo-ku, Tokyo 113-0033, Japan

<sup>4</sup>Materials Science and Engineering, College of Engineering, Shibaura Institute of Technology, 3-7-5 Toyosu, Koto-ku, Tokyo 135-8548, Japan

<sup>5</sup>Univ. Grenoble Alpes, CNRS, IPAG, 38000 Grenoble, France

<sup>6</sup>Institut de Radioastronomie Millimétrique, 38406 Saint-Martin d'Hères, France

<sup>7</sup>The Graduate University for Advanced Studies SOKENDAI, Shonan Village, Hayama, Kanagawa 240-0193, Japan

<sup>8</sup>Research Center for the Early Universe, The University of Tokyo, 7-3-1, Hongo, Bunkyo-ku, Tokyo 113-0033, Japan

Received 2023 November 1; revised 2024 May 12; accepted 2024 May 16; published 2024 July 12

## Abstract

Deuterium fractionation in the closest vicinity of a protostar is important in understanding its potential heritage to a planetary system. Here, we have detected the spectral line emission of CH<sub>3</sub>OH and its three deuterated species, CH<sub>2</sub>DOH, CHD<sub>2</sub>OH, and CH<sub>3</sub>OD, toward the low-mass protostellar source B335 at a resolution of 0''03 (5 au) with Atacama Large Millimeter/submillimeter Array. They have a ring distribution within the radius of 24 au with the intensity depression at the continuum peak. We derive the column densities and abundance ratios of the above species at six positions in the disk/envelope system as well as the continuum peak. The D/H ratio of CH<sub>3</sub>OH is ~[0.03–0.13], which is derived by correcting the statistical weight of 3 for CH<sub>2</sub>DOH. The [CHD<sub>2</sub>OH]/[CH<sub>2</sub>DOH] ratio is derived to be higher ([0.14–0.29]). On the other hand, the [CH<sub>2</sub>DOH]/[CH<sub>3</sub>OD] ratio ([4.9–15]) is higher than the statistical ratio of 3 and is comparable to those reported for other low-mass sources. We study the physical structure on a few astronomical unit scales in B335 by analyzing the CH<sub>3</sub>OH (18<sub>3,15</sub> – 18<sub>2,16</sub>, A) and HCOOH (12<sub>0,12</sub> – 11<sub>0,11</sub>) line emission. Velocity structures of these lines are reasonably explained as the infalling-rotating motion. The protostellar mass and the upper limit to the centrifugal barrier are thus derived to be 0.03–0.07 M<sub>☉</sub> and <7 au, respectively, showing that B335 harbors a young protostar with a tiny disk structure. Such youth of the protostar may be related to the relatively high [CH<sub>2</sub>DOH]/[CH<sub>3</sub>OH] ratio.

*Unified Astronomy Thesaurus concepts:* [Young stellar objects \(1834\)](#); [Star formation \(1569\)](#); [Protostars \(1302\)](#); [Interstellar molecules \(849\)](#); [Astrochemistry \(75\)](#)

## 1. Introduction

The simplest complex organic molecule, methanol (CH<sub>3</sub>OH), is widely observed toward protostellar sources to explore their chemical and physical structures. In star-forming clouds, it is thought to be formed through the hydrogenation of CO by H atoms on the dust grain surfaces in cold conditions during the prestellar phase (e.g., Watanabe & Kouchi 2002; Geppert et al. 2005; Fuchs et al. 2009). In this phase, desorption of CH<sub>3</sub>OH into the gas phase is limited to nonthermal processes such as surplus energy release of grain surface reactions (e.g., Garrod et al. 2007; Garrod & Widicus Weaver 2013). During the growth of the protostar, CH<sub>3</sub>OH is released into the gas phase in the inner envelope mainly through thermal desorption by protostellar heating. Therefore, the CH<sub>3</sub>OH emission is used as a tracer of hot core/corino around the protostar (e.g., Herbst & van Dishoeck 2009; Caselli & Ceccarelli 2012; Oya et al. 2016; Manigand et al. 2020; van Gelder et al. 2020; Imai et al. 2022; Ceccarelli et al. 2023; Okoda et al. 2023). The CH<sub>3</sub>OH emission is also observed in the outflow-shocked regions through sputtering and heating

processes (e.g., Bachiller & Pérez Gutiérrez 1997; Codella et al. 2020; Okoda et al. 2021).

Recent high-angular-resolution observations reveal the detailed distribution of the CH<sub>3</sub>OH emission. For instance, Oya et al. (2016) reported that the CH<sub>3</sub>OH emission in the low-mass protostellar source, IRAS 16293-2422 A, is enhanced in a ring-like structure of the innermost part of the infalling-rotating envelope, which corresponds to the transition zone between the envelope and the disk structure. Accretion shock and/or the geometrical effect favorable for protostar heating is proposed as the origin of enhancement (Oya & Yamamoto 2020). Accretion shock is also suggested for the enhancement of the CH<sub>3</sub>OH emission in some sources such as B335 (Okoda et al. 2022) and [BHB2007] 11 (Vastel et al. 2022). In short, studies on CH<sub>3</sub>OH emission provide us with important information connecting the chemical and physical structures of protostellar sources.

The deuterated species of CH<sub>3</sub>OH such as CH<sub>2</sub>DOH, CHD<sub>2</sub>OH, CD<sub>3</sub>OH, and CH<sub>3</sub>OD have also been detected in various protostellar sources. Generally, the D/H ratio of molecules (deuterium fractionation) reflects their formation processes as well as physical conditions and evolutionary stages. In fact, it has extensively been studied with observations of various deuterated species of not only CH<sub>3</sub>OH but also other molecules over the various regions, such as starless cores (e.g., Bizzocchi et al. 2014; Ambrose et al. 2021), both low-mass and high-mass protostars (e.g., Bianchi et al. 2017a, 2017b; Jørgensen et al. 2018; Taquet et al. 2019; Manigand et al.



Original content from this work may be used under the terms of the [Creative Commons Attribution 4.0 licence](#). Any further distribution of this work must maintain attribution to the author(s) and the title of the work, journal citation and DOI.

2020; Drozdovskaya et al. 2022; van Gelder et al. 2022; Yamato et al. 2024), and comets (e.g., Drozdovskaya et al. 2021; Müller et al. 2022). In these studies, the D/H ratios toward low-mass protostars are found to reach up to 10%.

In particular, the deuterium fractionation of CH<sub>3</sub>OH in various protostellar sources would be a key to understanding their physical and chemical evolution. Nevertheless, there still remain controversial issues on the CH<sub>3</sub>OH deuteration. For instance, previous observations suggested a systematic trend of the [CH<sub>2</sub>DOH]/[CH<sub>3</sub>OD] ratio between low-mass and high-mass protostellar sources. The ratio in low-mass protostellar sources tends to be higher than the statistical ratio of 3 (e.g., Bizzocchi et al. 2014; Jørgensen et al. 2018), whereas it is much lower than 3 in high-mass protostellar sources (e.g., Charnley et al. 1997; Belloche et al. 2016; Bøgelund et al. 2018; Wilkins & Blake 2022). Thus, more observational efforts for CH<sub>3</sub>OH and its deuterated species are awaited to understand the physical meaning of the ratio.

This paper is organized as follows. Our target is introduced in Section 2. Some key information on the observation is described in Section 3. In Section 4, we derive and discuss the column densities and the abundances of deuterated CH<sub>3</sub>OH in the disk/envelope system. We show the effect of  $S\mu^2$  on the column densities in Section 5. The distributions and velocity maps of the disk/envelope system are shown in Section 6. Using the infalling-rotating-envelope (IRE) model reported by Oya et al. (2022), we explore kinematics in the disk/envelope system in Section 7. In Section 8, we discuss the abundance ratios with those in other sources. We summarize the main results in Section 9.

## 2. Target: B335

B335 is a Bok globule (Keene et al. 1980), with which the Class 0 protostar IRAS 19347+0727 is associated. The bolometric temperature ( $T_{\text{bol}}$ ) is 37 K (Andre et al. 2000), while the bolometric luminosity ( $L_{\text{bol}}$ ) is 1.6  $L_{\odot}$  (Kang et al. 2021). The distance to B335 is reported to be 165 pc, based on the Gaia Data Release 2 parallax data (Watson 2020). In this paper, we employ this distance not only for our results but also for those in the previous works. We adjusted the physical parameter values of the previous works for the new distance (165 pc), since the studies before 2020 employed the distance to B335 of 100 pc, except for Yen et al. (2015) who employed 150 pc.

Extensive observations toward this isolated protostellar source have been carried out to develop star formation studies in terms of both physical and chemical structures (e.g., Hirano et al. 1988; Evans et al. 2015; Yen et al. 2015; Imai et al. 2016; Bjerkeli et al. 2019; Imai et al. 2019, 2022; Okoda et al. 2022). A bipolar outflow extending along the east-to-west direction (P.A.  $\sim 90^\circ$ ) was found (e.g., Hirano et al. 1988, 1992; Stutz et al. 2008; Bjerkeli et al. 2019; Cabedo et al. 2021), which is almost in parallel to the plane of the sky. Dedicated works have been reported on the physical properties of the disk/envelope system and the protostellar mass (Evans et al. 2015; Yen et al. 2015; Bjerkeli et al. 2019; Imai et al. 2019). The protostellar mass was estimated to be 0.06  $M_{\odot}$  from imperceptible rotation motion in the C<sup>18</sup>O line on the assumption of the infalling-rotating motion by Yen et al. (2015). Imai et al. (2019) clearly revealed a rotation motion around the protostar in the methanol (CH<sub>3</sub>OH) and formic acid (HCOOH) lines with a higher-resolution observation

( $\sim 0.1''$ ). They derived the protostellar mass and the radius of the centrifugal barrier to be 0.03–0.1  $M_{\odot}$  and  $< 8$  au, respectively, assuming the infalling-rotating motion. Meanwhile, the velocity gradient seen in the CH<sub>3</sub>OH and SO<sub>2</sub> lines is independently reported by Bjerkeli et al. (2019), where the results are consistent with a pure freefall or a Keplerian rotation with the protostellar mass of 0.08  $M_{\odot}$ . They also estimated the disk/envelope mass from the dust continuum emission within 12 au to be  $8 \times 10^{-4} M_{\odot}$ . In B335, a Keplerian disk is still veiled, although recent observations have found it around other young sources even in the Class 0/I stages (e.g., Ohashi et al. 2014; Aso et al. 2015; Okoda et al. 2018; Oya 2020). Bjerkeli (2023) implies that the disk structure just started to form in B335, based on the continuum observation.

The disk/envelope direction is close to the south-to-north axis. We employ the position angle (P.A.) of  $5^\circ$  for the disk/envelope direction in this paper (Figure 3(a)), based on the recent works observing a foot of the outflow with the Atacama Large Millimeter/submillimeter Array (ALMA; P.A.  $95^\circ$ : Bjerkeli et al. 2019; Cabedo et al. 2021). Bjerkeli et al. (2019, 2023) suggested the disk/envelope axis to be P.A.  $5^\circ$ , and Cabedo et al. (2021) reported it to be P.A.  $2^\circ$ . On the other hand, Oya et al. (2022) and Okoda et al. (2022) employed P.A.  $0^\circ$  to just take a consistent approach with Imai et al. (2019). However, only a  $5^\circ$  difference in the P.A. does not significantly affect any result.

Recently, CH<sub>3</sub>OH and CH<sub>2</sub>DOH were observed in B335 with ALMA at a high resolution of  $0.03''$  ( $\sim 5$  au at  $d = 165$  pc) by Okoda et al. (2022). In their study, the temperature structure in the disk/envelope system was the main focus by using CH<sub>3</sub>OH, CH<sub>2</sub>DOH, HCOOH, and NH<sub>2</sub>CHO line emission. The chemical differentiation among molecular distribution was also studied, based on the principal component analysis (PCA). They found that the CH<sub>3</sub>OH and deuterated CH<sub>3</sub>OH species (CH<sub>2</sub>DOH, CHD<sub>2</sub>OH, and CH<sub>3</sub>OD) have a ring-shaped and extended distribution. Their velocity structures most likely trace the disk/envelope system, while HCOOH, HNCO, and NH<sub>2</sub>CHO have a more compact distribution. Although the column densities of CH<sub>3</sub>OH and CH<sub>2</sub>DOH were derived simultaneously in the derivation of the temperature to show its variation along the major axis of the disk/envelope system, they were not discussed in terms of the D/H ratio. Since the intrinsic line intensities,  $S\mu^2$  ( $S$  is the line strength and  $\mu$  the dipole moment responsible for the transition: e.g., Yamamoto 2017), of CH<sub>2</sub>DOH in the database of JPL (Pickett et al. 1998) was recognized to be inaccurate for their observed transitions in B335, the analysis and discussion of the CH<sub>3</sub>OH deuteration including CHD<sub>2</sub>OH and CH<sub>3</sub>OD were left for a separate publication.

The  $S\mu^2$  value is directly related to the individual line intensity and is an important parameter in the line analysis (the details are described elsewhere, e.g., Yamamoto 2017; Oyama et al. 2023). Since the  $S\mu^2$  values of CH<sub>2</sub>DOH were recently measured with the laboratory experiment (Oyama et al. 2023) and those of CHD<sub>2</sub>OH with the theoretical calculation (Coudert et al. 2021, See also Drozdovskaya et al. 2022), reliable derivations of their column densities are now possible by making use of them. In this paper, we study the CH<sub>3</sub>OH deuteration and the velocity structure of the disk/envelope system within a few 10 au scale.

**Table 1**  
Analyzed Molecular Lines<sup>a</sup>

Molecule	Transition	Frequency (GHz)	$S\mu^2$ <sup>b</sup> ( $D^2$ )	$S\mu^2$ <sub>SUMIRE</sub> <sup>c</sup> ( $D^2$ )	$\log_{10} A$ <sup>d</sup>	$\log_{10} A_{\text{SUMIRE}}$ <sup>e</sup>	$E_u$ $k^{-1}$ (K)	Synthesized Beam Size
CH <sub>3</sub> OH	18 <sub>3,15</sub> – 18 <sub>2,16</sub> , A	247.610918	17.358	...	–4.081	...	446.6	0''033×0''027 (P.A. –2°6)
CH <sub>3</sub> OH	21 <sub>3,18</sub> – 21 <sub>2,19</sub> , A	245.223019	20.623	...	–4.084	...	585.8	0''033×0''028 (P.A. –6°9)
CH <sub>3</sub> OH	12 <sub>6,7</sub> – 13 <sub>5,8</sub> , E	261.704409	2.131	...	–4.75	...	359.8	0''032×0''026 (P.A. 4°6)
CH <sub>3</sub> OH	17 <sub>3,14</sub> – 17 <sub>2,15</sub> , A	248.282424	16.315	...	–4.081	...	404.8	0''032×0''026 (P.A. –9°4)
CH <sub>3</sub> OH	4 <sub>2,2</sub> – 5 <sub>1,5</sub> , A	247.228587	1.086	...	–4.673	...	60.9	0''033×0''027 (P.A. –5°1)
CH <sub>3</sub> OH	2 <sub>1,1</sub> – 1 <sub>0,1</sub> , E	261.805675	1.334	...	–4.254	...	28.0	0''032×0''026 (P.A. 4°3)
CH <sub>2</sub> DOH	10 <sub>2,8</sub> – 10 <sub>1,9</sub> , o <sub>1</sub>	244.9888456	3.439	2.22	–4.552	–4.74	153.3	0''033×0''028 (P.A. –7°4)
CH <sub>2</sub> DOH	4 <sub>2,2</sub> – 4 <sub>1,3</sub> , e <sub>0</sub>	244.8411349	2.540	1.80	–4.317	–4.47	37.6	0''033×0''028 (P.A. –7°5)
CH <sub>2</sub> DOH	5 <sub>2,4</sub> – 5 <sub>1,5</sub> , e <sub>0</sub>	261.6873662	4.006	3.01	–4.119	–4.24	48.3	0''032×0''026 (P.A. 4°6)
CH <sub>2</sub> DOH	3 <sub>2,1</sub> – 3 <sub>1,2</sub> , e <sub>0</sub>	247.6257463	2.360	1.68	–4.225	–4.37	29.0	0''033×0''027 (P.A. –2°6)
CHD <sub>2</sub> OH <sup>f</sup>	6 <sub>1,1</sub> – 5 <sub>1,1</sub> , o <sub>1</sub>	246.1432950	4.821	5.22	–4.191	–4.16	52.9	0''033×0''027 (P.A. –4°4)
CHD <sub>2</sub> OH <sup>f</sup>	6 <sub>1,2</sub> – 5 <sub>1,2</sub> , e <sub>0</sub>	246.2530390	4.759	5.36	–4.196	–4.14	44.6	0''033×0''027 (P.A. –4°4)
CHD <sub>2</sub> OH <sup>f</sup>	4 <sub>1,2</sub> – 4 <sub>0,1</sub> , o <sub>1</sub> -e <sub>0</sub>	247.2524160	5.655	6.86	–3.956	–3.87	31.8	0''032×0''027 (P.A. –7°7)
CH <sub>3</sub> OD	5 <sub>1</sub> – 4 <sub>0</sub> , E	245.142988	3.8	...	–4.8	...	37.3	0''033×0''028 (P.A. –6°9)
HCOOH	12 <sub>0,12</sub> – 11 <sub>0,11</sub>	262.1034810	24.157	...	–3.694	...	82.8	0''032×0''026 (P.A. 4°4)

### Notes.

<sup>a</sup> Line parameters are taken from CDMS (Endres et al. 2016) and JPL (Pickett et al. 1998) except for CH<sub>3</sub>OD. The parameters for CH<sub>3</sub>OD are taken from Anderson et al. (1988) and Duan et al. (2003).

<sup>b</sup> Taken from CDMS for CH<sub>3</sub>OH and CHD<sub>2</sub>OH and calculated from the intensity listed in JPL for CH<sub>2</sub>DOH. For CH<sub>3</sub>OD, we employ the data reported by Anderson et al. (1988).

<sup>c</sup> Taken from Oyama et al. (2023) for CH<sub>2</sub>DOH. Provided by T. Oyama for CHD<sub>2</sub>OH. These values are the experimental data. The uncertainty is 10% for the  $S\mu^2$ <sub>SUMIRE</sub> value.

<sup>d</sup> Einstein coefficients calculated from  $S\mu^2$ <sub>JPL</sub> or  $S\mu^2$ <sub>CDMS</sub>.

<sup>e</sup> Einstein coefficients calculated from  $S\mu^2$ <sub>SUMIRE</sub>.

<sup>f</sup> The quantum numbers follow the definition of CDMS.

## 3. Observation

Single-point ALMA observations toward B335 were carried out with the Band 6 receiver in the four execution blocks of the Cycle 6 operation on 2019 June 10, 12, 13, and 23. The molecular lines analyzed in this paper are summarized in Table 1. The line at 247.2524160 GHz is newly identified in this paper as the CHD<sub>2</sub>OH (4<sub>1,2</sub>–4<sub>0,1</sub>, o<sub>1</sub>-e<sub>0</sub>) line, based on the spectroscopic data by Couderc et al. (2021) and the database of CDMS (Endres et al. 2016). Since the maximum recoverable scale is 0''3 for these observations, we here focus on the small-scale structure around the protostar. The synthesized beam size for each line is summarized in Table 1. The spectral resolution is 0.544–0.691 km s<sup>–1</sup>, and the rms noise is 1.0 mJy beam<sup>–1</sup>channel<sup>–1</sup>. Further observation parameters (calibrators, primary beamwidth, correlator setups, etc.) are described elsewhere (Okoda et al. 2022).

The data reduction was performed with the Common Astronomy Software Applications package 5.8.0 (McMullin et al. 2007) as well as a modified version of the ALMA calibration pipeline. We combined four visibility data in the  $uv$  plane after phase self-calibration using each continuum data and the application of their solution to the spectral line data.

## 4. Deuterated CH<sub>3</sub>OH Species in the Disk/Envelope System

We here analyze the CH<sub>3</sub>OH, CH<sub>2</sub>DOH, CHD<sub>2</sub>OH, and CH<sub>3</sub>OD lines listed in Table 1 to study the deuterium fractionation of CH<sub>3</sub>OH in the disk/envelope system. Figure 1 shows the moment zero maps of the CH<sub>3</sub>OH (18<sub>3,15</sub> – 18<sub>2,16</sub>, A), CH<sub>2</sub>DOH (4<sub>2,2</sub> – 4<sub>1,3</sub>, e<sub>0</sub>), CHD<sub>2</sub>OH (4<sub>1,2</sub> – 4<sub>0,1</sub>, o<sub>1</sub>-e<sub>0</sub>), and CH<sub>3</sub>OD (5<sub>1,4</sub>, E) lines with the synthesized beam size (0''030×0''023; Table 1). They have a ring-shaped distribution around the protostar with the intensity depression at the

continuum peak due to the high dust opacity. Similar images are also reported for the CH<sub>3</sub>OH, CH<sub>2</sub>DOH, and CH<sub>3</sub>OD lines by Okoda et al. (2022), where the beam sizes are smoothed to be 0''034 to perform the PCA.

Okoda et al. (2022) derived the column densities of CH<sub>3</sub>OH and CH<sub>2</sub>DOH with each aperture of 0''03 for 9 positions along the midplane of the envelope (P.A. 0°) using the  $S\mu^2$  values calculated from the line intensities listed in the database of JPL. A recent experimental measurement for some lines of CH<sub>2</sub>DOH with SUMIRE (Spectrometer Using superconductor MIXer REceiver) by Oyama et al. (2023) found that the  $S\mu^2$  values in the database of JPL significantly deviate from the measured values. The experimental  $S\mu^2$  values for some lines of CHD<sub>2</sub>OH are now available with SUMIRE very recently (Oyama et al. in prep). In the following, we first derive the column densities and abundances of CH<sub>2</sub>DOH and CHD<sub>2</sub>OH by using the newly available experimental  $S\mu^2$  values (hereafter referred to as  $S\mu^2$ <sub>SUMIRE</sub>) listed in Table 1. We discuss the dependence of the gas temperature and the column densities on the  $S\mu^2$  values later (Section 5).

### 4.1. Column Densities

We derive the column densities of CH<sub>3</sub>OH and deuterated CH<sub>3</sub>OH species toward seven rectangle areas (0''03×0''05) along the disk/envelope direction (P.A. 5°) including the continuum peak position, as shown in Figure 1(a). The rectangle shape is here employed to obtain the spectra with the high signal-to-noise ratio as much as possible for the disk/envelope system with the apparently thick disk height. For our derivation, we use the same equations as those reported by Okoda et al. (2022), assuming the local thermodynamic equilibrium (LTE) condition (Appendix A). In this analysis,

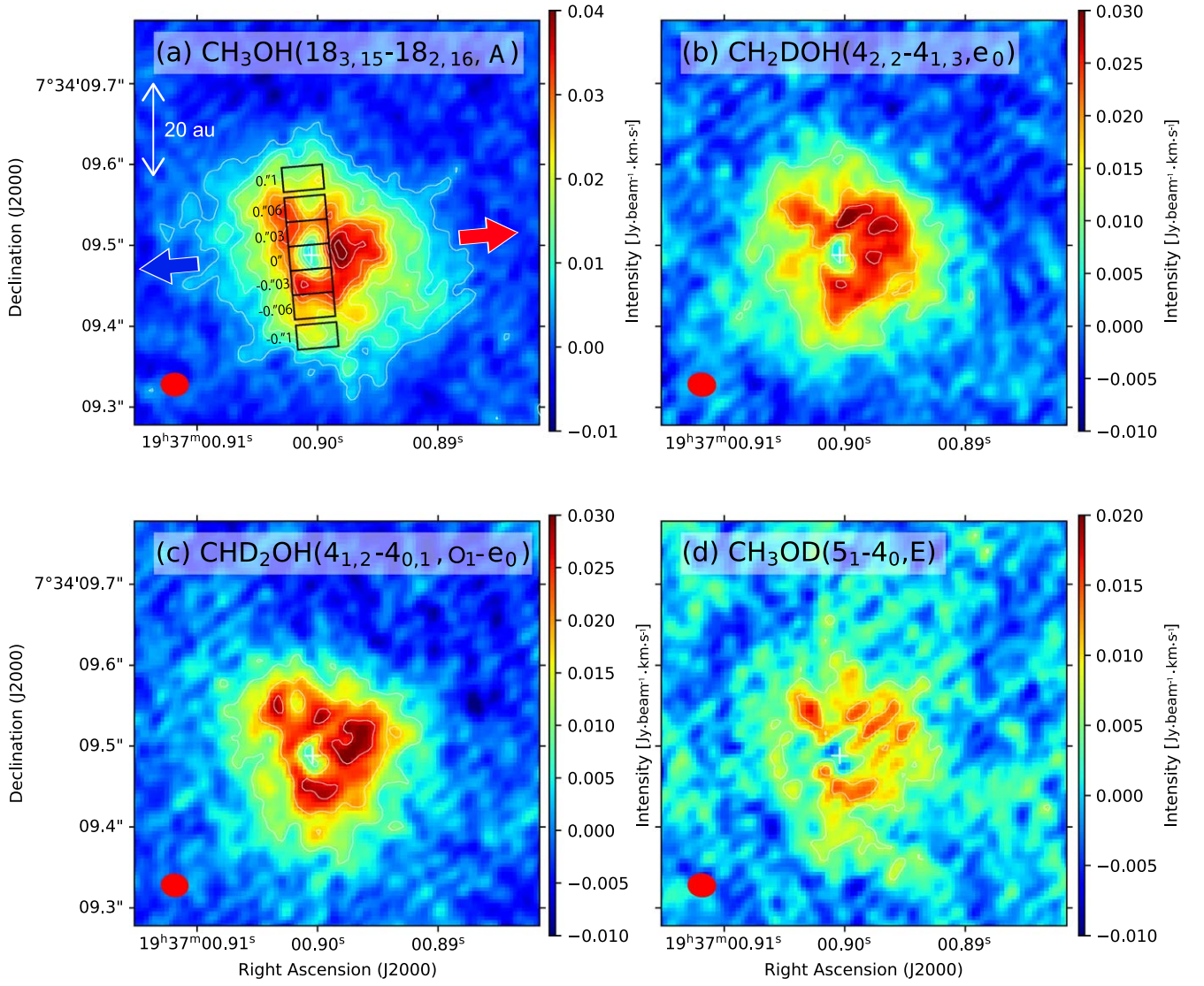


**Figure 1.** Moment zero maps of the  $\text{CH}_3\text{OH}$  ( $18_{3,15} - 18_{2,16}$ , A,  $E_u = 447$  K),  $\text{CH}_2\text{DOH}$  ( $4_{2,2} - 4_{1,3}$ ,  $e_0$ ,  $E_u = 38$  K),  $\text{CHD}_2\text{OH}$  ( $4_{1,2} - 4_{0,1}$ ,  $o_1 - e_0$ ,  $E_u = 32$  K), and  $\text{CH}_3\text{OD}$  ( $5_{1,4_0}$ , E,  $E_u = 37$  K) emission. The integrated velocity range is from  $-0.2 \text{ km s}^{-1}$  to  $14.5 \text{ km s}^{-1}$ . The systemic velocity is  $8.34 \text{ km s}^{-1}$  (Yen et al. 2015). Contour levels are every  $3\sigma$  from  $3\sigma$ , where  $\sigma$  is  $1.5 \text{ mJy beam}^{-1}$ ,  $3.0 \text{ mJy beam}^{-1}$ ,  $3.0 \text{ mJy beam}^{-1}$ , and  $2.0 \text{ mJy beam}^{-1}$ , respectively. The spectra are obtained within each rectangle area ( $0''.03 \times 0''.05$ ) to calculate the temperature and the column density. The numbers represent the offsets from the continuum peak ( $0''/0$ ). The white cross mark shows the continuum peak position  $(\alpha_{2000}, \delta_{2000}) = (19^{\text{h}}37^{\text{m}}00^{\text{s}}.90, +7^{\circ}34'09''.49)$ . The red ellipse in each map represents the beam size. The red and blue arrows in panel (a) show the directions of the red- and blueshifted outflow.

we focus on the disk/envelope system within 20 au in radius from the protostar. The LTE analysis is justified, since the  $\text{H}_2$  density for that area is roughly estimated to be higher than  $10^8 \text{ cm}^{-3}$ , based on its apparent size and the  $\text{H}_2$  column density of  $5.66 \times 10^{23} \text{ cm}^{-2}$  reported by Imai et al. (2016). In addition, the  $\text{CH}_3\text{OH}$  emission in our observation selectively traces the warm/hot region because of the maximum recoverable scale of  $0''.3$ . In the derivation, the optical depths of molecular lines and dust emission are considered by assuming that the gas and dust are well mixed and the gas temperature is equal to the dust temperature. Since the dust continuum emission is intense, we take its effect into the analysis approximately (Appendix A).

The best-fit temperatures and column densities are summarized in Table 2, where the errors are evaluated by the  $\chi^2$  analysis. The offset in Table 2 means the distance from the protostar along the midplane of the disk/envelope system from the southwestern to the northeastern direction (P.A.  $5^\circ$ ), where the offset of  $0''.1$  ( $\sim 17$  au) is almost close to the edge of the

distributions of  $\text{CH}_3\text{OH}$  and its deuterated species. Examples of the line parameters of  $\text{CH}_3\text{OH}$  at the offset of  $-0''.03$  used for the analysis are shown in Appendix B. As the upper-state energies of the observed lines of  $\text{CHD}_2\text{OH}$  are close to one another and there is only one line of  $\text{CH}_3\text{OD}$  in our setup, we cannot determine the temperature independently for these two species. Therefore, in the calculation of the column densities of  $\text{CHD}_2\text{OH}$  and  $\text{CH}_3\text{OD}$ , we assume the  $\text{CH}_3\text{OH}$  temperature obtained for each position, considering the coexisting nature of  $\text{CH}_3\text{OH}$  and its isotopologues (see Figure 1). In addition, the temperature of  $\text{CH}_3\text{OH}$  is better determined than that of  $\text{CH}_2\text{DOH}$  due to the higher signal-to-noise ratio. For  $\text{CH}_3\text{OD}$ , we employ the  $S\mu^2$  value calculated by Anderson et al. (1988).

At the continuum peak, the observed column densities of  $\text{CH}_3\text{OH}$  and its isotopologues are seriously affected by the high optical depth of dust continuum emission, as revealed by the central dip of the images in Figure 1. Only a lower limit can be derived for the column density of  $\text{CH}_2\text{DOH}$

**Table 2**  
Temperatures and Column Densities in the Disk/Envelope System

Molecules	Offsets <sup>a</sup>	$S\mu_{\text{JPL}}^2$ or $S\mu_{\text{CDMS}}^2$ <sup>c</sup>		$S\mu_{\text{SUMIRE}}^2$	
		$T$ (K)	$N$ ( $10^{18} \text{ cm}^{-2}$ )	$T$ (K)	$N$ ( $10^{18} \text{ cm}^{-2}$ )
CH <sub>3</sub> OH <sup>b</sup>	0.1	107 <sup>+2</sup> <sub>-2</sub>	4.4 <sup>+0.5</sup> <sub>-0.3</sub>	...	...
	0.06	142 <sup>+3</sup> <sub>-4</sub>	9.0 <sup>+3.0</sup> <sub>-1.7</sub>	...	...
	0.03	164 <sup>+6</sup> <sub>-6</sub>	>9.6	...	...
	0 <sup>d</sup>	217 <sup>+2</sup> <sub>-2</sub>	11 <sup>+5</sup> <sub>-2</sub>	...	...
	-0.03	186 <sup>+2</sup> <sub>-2</sub>	13 <sup>+4</sup> <sub>-3</sub>	...	...
	-0.06	146 <sup>+4</sup> <sub>-3</sub>	8.0 <sup>+1.7</sup> <sub>-1.3</sub>	...	...
	-0.1	124 <sup>+3</sup> <sub>-3</sub>	3.7 <sup>+1.1</sup> <sub>-0.8</sub>	...	...
CH <sub>2</sub> DOH <sup>b</sup>	0.1	72 <sup>+3</sup> <sub>-1</sub>	0.47 <sup>+0.06</sup> <sub>-0.06</sub>	72 <sup>+2</sup> <sub>-2</sub>	0.74 <sup>+0.10</sup> <sub>-0.10</sub>
	0.06	119 <sup>+12</sup> <sub>-8</sub>	0.85 <sup>+0.09</sup> <sub>-0.06</sub>	118 <sup>+8</sup> <sub>-8</sub>	1.2 <sup>+0.2</sup> <sub>-0.1</sub>
	0.03	143 <sup>+3</sup> <sub>-3</sub>	2.6 <sup>+0.9</sup> <sub>-0.4</sub>	143 <sup>+3</sup> <sub>-3</sub>	3.8 <sup>+0.9</sup> <sub>-0.6</sub>
	0 <sup>d</sup>	188 <sup>+8</sup> <sub>-6</sub>	>3.5	188 <sup>+8</sup> <sub>-4</sub>	>5.2
	-0.03	162 <sup>+12</sup> <sub>-8</sub>	2.5 <sup>+0.8</sup> <sub>-0.4</sub>	161 <sup>+8</sup> <sub>-6</sub>	3.6 <sup>+1.1</sup> <sub>-0.6</sub>
	-0.06	135 <sup>+30</sup> <sub>-16</sub>	1.00 <sup>+0.20</sup> <sub>-0.11</sub>	132 <sup>+22</sup> <sub>-12</sub>	1.5 <sup>+0.3</sup> <sub>-0.2</sub>
	-0.1	106 <sup>+36</sup> <sub>-14</sub>	0.52 <sup>+0.26</sup> <sub>-0.10</sub>	104 <sup>+26</sup> <sub>-12</sub>	0.79 <sup>+0.41</sup> <sub>-0.18</sub>
CHD <sub>2</sub> OH <sup>c</sup>	0.1	107 <sup>+15</sup> <sub>-15</sub>	0.15 <sup>+0.02</sup> <sub>-0.02</sub>	107 <sup>+15</sup> <sub>-15</sub>	0.13 <sup>+0.02</sup> <sub>-0.02</sub>
	0.06	142 <sup>+15</sup> <sub>-15</sub>	0.35 <sup>+0.04</sup> <sub>-0.03</sub>	142 <sup>+15</sup> <sub>-15</sub>	0.31 <sup>+0.03</sup> <sub>-0.03</sub>
	0.03	164 <sup>+15</sup> <sub>-15</sub>	0.71 <sup>+0.05</sup> <sub>-0.01</sub>	164 <sup>+15</sup> <sub>-15</sub>	0.629 <sup>+0.042</sup> <sub>-0.002</sub>
	0 <sup>d</sup>	217 <sup>+15</sup> <sub>-15</sub>	1.2 <sup>+0.6</sup> <sub>-0.2</sub>	217 <sup>+15</sup> <sub>-15</sub>	1.1 <sup>+0.4</sup> <sub>-0.2</sub>
	-0.03	186 <sup>+15</sup> <sub>-15</sub>	<0.77	186 <sup>+15</sup> <sub>-15</sub>	<0.68
	-0.06	146 <sup>+15</sup> <sub>-15</sub>	0.35 <sup>+0.03</sup> <sub>-0.02</sub>	146 <sup>+15</sup> <sub>-15</sub>	0.31 <sup>+0.03</sup> <sub>-0.02</sub>
	-0.1	124 <sup>+15</sup> <sub>-15</sub>	0.20 <sup>+0.02</sup> <sub>-0.01</sub>	124 <sup>+15</sup> <sub>-15</sub>	0.17 <sup>+0.02</sup> <sub>-0.01</sub>
CH <sub>3</sub> OD <sup>c</sup>	0.1	107 <sup>+15</sup> <sub>-15</sub>	0.06 <sup>+0.01</sup> <sub>-0.01</sub>	...	...
	0.06	142 <sup>+15</sup> <sub>-15</sub>	0.22 <sup>+0.02</sup> <sub>-0.03</sub>	...	...
	0.03	164 <sup>+15</sup> <sub>-15</sub>	<0.34	...	...
	0 <sup>d</sup>	217 <sup>+15</sup> <sub>-15</sub>	2.0 <sup>+0.5</sup> <sub>-0.3</sub>	...	...
	-0.03	186 <sup>+15</sup> <sub>-15</sub>	0.45 <sup>+0.02</sup> <sub>-0.01</sub>	...	...
	-0.06	146 <sup>+15</sup> <sub>-15</sub>	0.19 <sup>+0.02</sup> <sub>-0.02</sub>	...	...
	-0.1	124 <sup>+15</sup> <sub>-15</sub>	0.11 <sup>+0.01</sup> <sub>-0.01</sub>	...	...

#### Notes.

<sup>a</sup> Offsets from the continuum peak position along the envelope (P.A. 5°).

<sup>b</sup> The errors are estimated by using the  $\chi^2$  analysis.

<sup>c</sup> These temperatures are assumed to be that of CH<sub>3</sub>OH. For the error estimation of CHD<sub>2</sub>OH and CH<sub>3</sub>OD, we assume the temperature error of  $\pm 15$  K. These values are derived from the spectra for the rectangle area (0''03 $\times$ 0''05) shown in Figure 1(a).

<sup>d</sup> At the continuum peak, the observed column densities are seriously affected by the high optical depth of dust continuum emission, and hence, we focus on the values at the six positions in the envelope in this paper.

<sup>e</sup> For CH<sub>2</sub>DOH and CHD<sub>2</sub>OH, the column densities are calculated with the  $S\mu_{\text{JPL}}^2$  and  $S\mu_{\text{CDMS}}^2$  values, respectively.

(>5.2  $\times 10^{18} \text{ cm}^{-2}$ ), while those of CHD<sub>2</sub>OH and CH<sub>3</sub>OD are derived to be 1.1<sup>+0.4</sup><sub>-0.2</sub>  $\times 10^{18} \text{ cm}^{-2}$  and 2.0<sup>+0.5</sup><sub>-0.3</sub>  $\times 10^{18} \text{ cm}^{-2}$ , respectively. Therefore, we mainly focus on the column densities at the six positions in the envelope. Among three deuterated species, CH<sub>2</sub>DOH shows the highest column density at all positions, which is in the range of [0.61–4.7]  $\times 10^{18} \text{ cm}^{-2}$ . The column densities of CHD<sub>2</sub>OH and CH<sub>3</sub>OD are in the range of [0.11–0.67]  $\times 10^{18} \text{ cm}^{-2}$  and [0.05–0.47]  $\times 10^{18} \text{ cm}^{-2}$ , respectively. Within the radius of 0''1, the column densities of all species seem to decrease as an increasing offset. The errors are estimated by using the  $\chi^2$  analysis for CH<sub>3</sub>OH and CH<sub>2</sub>DOH, where 1 $\sigma$  uncertainty is presented as the error for each parameter. For CHD<sub>2</sub>OH and

CH<sub>3</sub>OD, we estimate the errors of their column densities, based on the assumed temperature range of  $\pm 15$  K from the CH<sub>3</sub>OH temperature.

#### 4.2. Abundances

Using these derived column densities (Table 2), we derive the five abundance ratios: [CH<sub>2</sub>DOH]/[CH<sub>3</sub>OH], [CHD<sub>2</sub>OH]/[CH<sub>3</sub>OH], [CH<sub>3</sub>OD]/[CH<sub>3</sub>OH], [CH<sub>2</sub>DOH]/[CH<sub>3</sub>OD], and [CHD<sub>2</sub>OH]/[CH<sub>2</sub>DOH] (Figure 2 and Table 3). As seen in Figure 2, the abundance ratios do not reveal any systematic variation. Rather, they are roughly constant over the envelope (see also Table 3). At the continuum peak, all of the ratios have large uncertainties or just the lower and upper limits due to high dust opacity. The [CH<sub>2</sub>DOH]/[CH<sub>3</sub>OH], [CHD<sub>2</sub>OH]/[CH<sub>3</sub>OH], and [CH<sub>3</sub>OD]/[CH<sub>3</sub>OH] ratios in the envelope are in the range of [0.09–0.38], [0.02–0.06], and [0.011–0.06], respectively (Figures 2(a), (b), and (c)). In Figures 2(d) and (e), the [CH<sub>2</sub>DOH]/[CH<sub>3</sub>OD] and [CHD<sub>2</sub>OH]/[CH<sub>2</sub>DOH] ratios are in the range of [4.9–15] and [0.14–0.29], respectively (see also Table 3). We discuss the [CH<sub>2</sub>DOH]/[CH<sub>3</sub>OH], [CHD<sub>2</sub>OH]/[CH<sub>2</sub>DOH], and [CH<sub>2</sub>DOH]/[CH<sub>3</sub>OD] ratios in Section 8. Although the column densities and the abundances are roughly constant over the disk/envelope system, the temperatures of CH<sub>3</sub>OH and CH<sub>2</sub>DOH decrease with increasing distance from the protostar position.

The dust optical depths ( $\tau_{\text{dust}}$ ) are summarized in Appendix C. Note that the  $\tau_{\text{dust}}$  values obtained in the analyses of the CH<sub>3</sub>OH and CH<sub>2</sub>DOH lines are slightly different for some positions due to the different temperatures. If we employ the CH<sub>3</sub>OH temperature for the calculation of CH<sub>2</sub>DOH, its column density is (0.44–2.8)  $\times 10^{18} \text{ cm}^{-2}$  in the disk/envelope system, and the lower limits to the abundance ratios are higher than those when the CH<sub>2</sub>DOH temperature is employed. In short, the different treatments of the CH<sub>2</sub>DOH temperature do not seriously affect the trend as discussed in Section 8.

#### 5. An Effect of $S\mu^2$ on the Column Densities

In the previous section, we use the experimental value,  $S\mu_{\text{SUMIRE}}^2$ , for the derivation of the column density of CH<sub>2</sub>DOH and CHD<sub>2</sub>OH. Since the derived column density and rotation temperature depend on the  $S\mu^2$  values used, we here note the effects on the results for the different  $S\mu^2$  values for the CH<sub>2</sub>DOH ( $S\mu_{\text{SUMIRE}}^2$  versus  $S\mu_{\text{JPL}}^2$ ) and CHD<sub>2</sub>OH ( $S\mu_{\text{SUMIRE}}^2$  versus  $S\mu_{\text{CDMS}}^2$ ) lines. In Table 1, column four represents the  $S\mu^2$  values calculated from the line intensity in the database of JPL (hereafter referred to as  $S\mu_{\text{JPL}}^2$ ) for the CH<sub>2</sub>DOH lines and those taken from the database of CDMS (hereafter referred to as  $S\mu_{\text{CDMS}}^2$ ) for the CHD<sub>2</sub>OH lines.

The differences between  $S\mu_{\text{JPL}}^2$  and  $S\mu_{\text{SUMIRE}}^2$  are conspicuous for CH<sub>2</sub>DOH:  $S\mu_{\text{SUMIRE}}^2$  is 0.6–0.8 times smaller than  $S\mu_{\text{JPL}}^2$ . The temperature and the column density toward the offset of -0''03 from the continuum peak are derived with  $S\mu_{\text{JPL}}^2$  to be 162<sup>+12</sup><sub>-8</sub> K and 2.5<sup>+0.8</sup><sub>-0.4</sub>  $\times 10^{18} \text{ cm}^{-2}$ , respectively. When we use  $S\mu_{\text{SUMIRE}}^2$ , they are derived to be 161<sup>+8</sup><sub>-6</sub> K and 3.6<sup>+1.1</sup><sub>-0.6</sub>  $\times 10^{18} \text{ cm}^{-2}$ , respectively. The former column density is about 1.4 times smaller than the latter column density, while the temperatures are almost the same as each other. At the other positions, the column densities of CH<sub>2</sub>DOH derived with  $S\mu_{\text{JPL}}^2$  is also 1.4–1.6 times smaller than those derived with  $S\mu_{\text{SUMIRE}}^2$ , as shown in Table 2, resulting in the range of the column densities and the ratios as:  $N(\text{CH}_2\text{DOH}) = [0.41-$

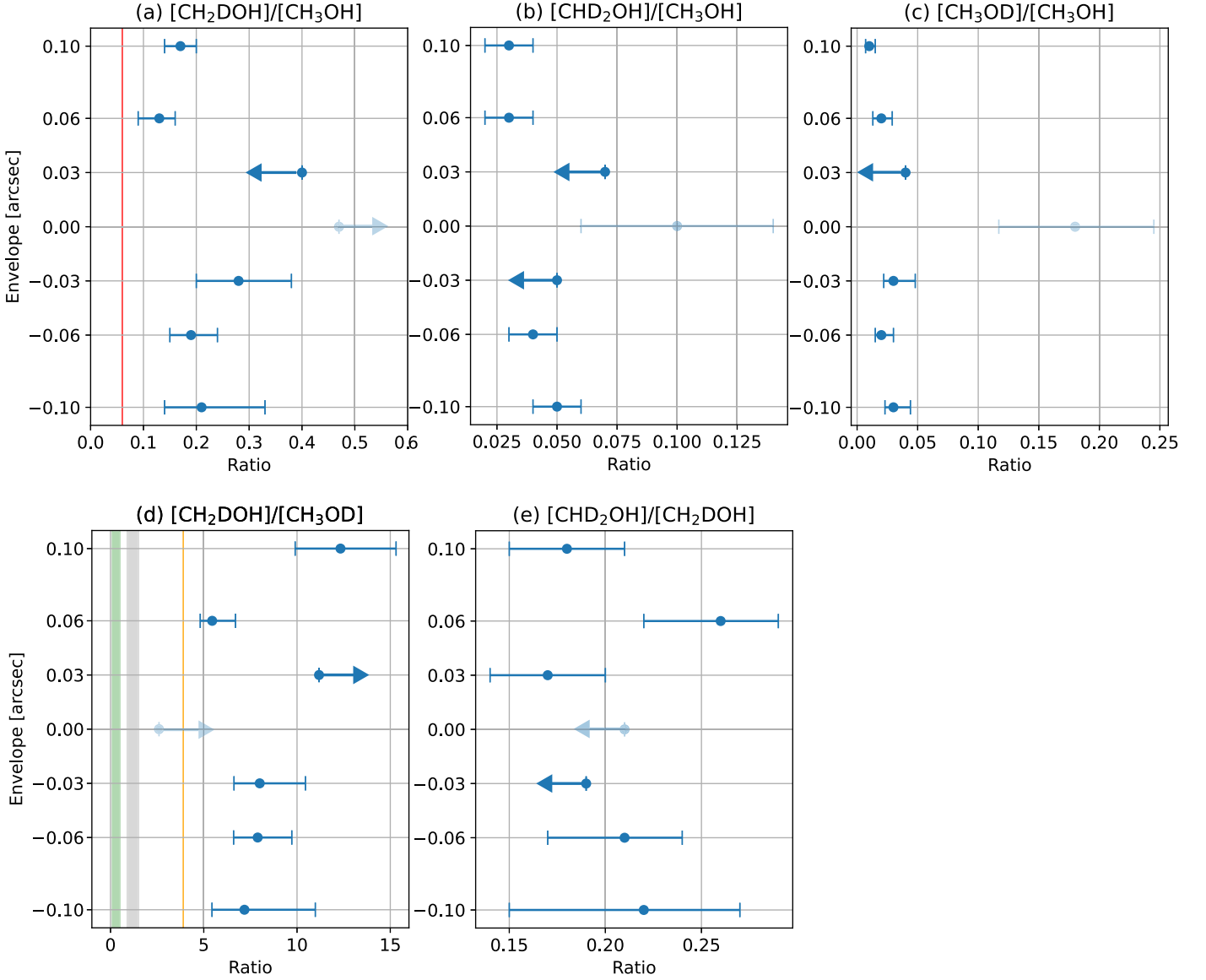


**Figure 2.** (a)–(e) Abundance ratios along the envelope (P.A.  $5^\circ$ ). Column densities of  $\text{CH}_2\text{DOH}$  and  $\text{CHD}_2\text{OH}$  derived from  $S\mu^2_{\text{SUMIRE}}$  are employed here. At the continuum peak, the observed column densities are seriously affected by the high optical depth of dust continuum emission, and hence, we focus on the abundances at the six positions in the envelope in this paper. The left and right arrows show the upper and lower limits of the abundance ratios, respectively. (a) The red vertical line represents the average in low-mass protostars (0.06) reported by van Gelder et al. (2022). (d) The ratio in the low-mass protostellar source IRAS 16293-2422 B (3.9) is shown in the orange vertical line for comparison (Jørgensen et al. 2018). Green and gray areas indicate the ratios in high-mass sources NGC 6334 I (0.1–0.5; Bøgelund et al. 2018) and Orion KL (0.9–1.5; Peng et al. 2012; Neill et al. 2013), respectively.

$3.5 \times 10^{18} \text{ cm}^{-2}$ ,  $[\text{CH}_2\text{DOH}]/[\text{CH}_3\text{OH}] = [0.07\text{--}0.26]$ , and  $[\text{CH}_2\text{DOH}]/[\text{CH}_3\text{OD}] = [3.5\text{--}9.7]$ . Note that some of the  $\text{CH}_2\text{DOH}$  column densities are different from those reported by Okoda et al. (2022) beyond the errors and the effect of the  $S\mu^2$  difference, particularly at the continuum peak position. This is because the circle area with a diameter of  $0''.03$  was employed for their derivation.

On the other hand, the difference between  $S\mu^2_{\text{CDMS}}$  and  $S\mu^2_{\text{SUMIRE}}$  for the  $\text{CHD}_2\text{OH}$  lines is relatively small (Table 1). The  $S\mu^2_{\text{SUMIRE}}$  values are about 1.2 times larger than the  $S\mu^2_{\text{CDMS}}$  values at most for the observed lines. In this case, the upper limits to the column densities at the offset of  $-0''.03$  are similar to each other: they are  $<0.77 \times 10^{18} \text{ cm}^{-2}$  and  $<0.68 \times 10^{18} \text{ cm}^{-2}$  with the  $S\mu^2_{\text{CDMS}}$  and  $S\mu^2_{\text{SUMIRE}}$  values, respectively, where we assume the  $\text{CH}_3\text{OH}$  temperature of  $186 \pm 15 \text{ K}$ . Therefore, a choice of the  $S\mu^2_{\text{CDMS}}$  and  $S\mu^2_{\text{SUMIRE}}$

values does not cause serious differences on the abundance ratios in our observation (Table 3). The  $[\text{CHD}_2\text{OH}]/[\text{CH}_2\text{DOH}]$  ratio is mostly affected by the difference in the  $S\mu^2$  value of  $\text{CH}_2\text{DOH}$ . Using the  $S\mu^2_{\text{JPL}}$  value for  $\text{CH}_2\text{DOH}$  and the  $S\mu^2_{\text{CDMS}}$  value for  $\text{CHD}_2\text{OH}$ , we obtain  $[0.20\text{--}0.46]$  (Table 3).

It should be noted that the effect of  $S\mu^2$  values on the column densities depends on which lines are used for the derivation. In other words, different lines have different differences between the  $S\mu^2_{\text{JPL}}$  and  $S\mu^2_{\text{SUMIRE}}$  values or between the  $S\mu^2_{\text{CDMS}}$  and  $S\mu^2_{\text{SUMIRE}}$  values. Therefore, an effect of the  $S\mu^2$  values on the column densities in any other observations would be different from those reported here. Thus, we need special care for a comparison of column densities and their ratios with those in other sources reported previously.

**Table 3**  
Abundance Ratios in the Disk/Envelope System

$S\mu_{\text{JPL}}^2$ or $S\mu_{\text{CDMS}}^2$ <sup>a</sup>	Offset <sup>b</sup>	[CH <sub>2</sub> DOH]/[CH <sub>3</sub> OH]	[CHD <sub>2</sub> OH]/[CH <sub>3</sub> OH]	[CH <sub>3</sub> OD]/[CH <sub>3</sub> OH]	[CH <sub>2</sub> DOH]/[CH <sub>3</sub> OD]	[CHD <sub>2</sub> OH]/[CH <sub>2</sub> DOH]
	0.1	0.11 <sup>+0.02</sup> <sub>-0.02</sub>	0.03 <sup>+0.01</sup> <sub>-0.01</sub>	0.014 <sup>+0.005</sup> <sub>-0.003</sub>	7.8 <sup>+1.9</sup> <sub>-1.5</sub>	0.32 <sup>+0.06</sup> <sub>-0.06</sub>
	0.06	0.09 <sup>+0.02</sup> <sub>-0.02</sub>	0.04 <sup>+0.01</sup> <sub>-0.01</sub>	0.024 <sup>+0.008</sup> <sub>-0.007</sub>	3.9 <sup>+0.7</sup> <sub>-0.4</sub>	0.41 <sup>+0.05</sup> <sub>-0.05</sub>
	0.03	<0.27	<0.07	<0.04	>7.7	0.27 <sup>+0.04</sup> <sub>-0.07</sub>
	0 <sup>e</sup>	>0.32	0.11 <sup>+0.06</sup> <sub>-0.04</sub>	0.18 <sup>+0.06</sup> <sub>-0.06</sub>	>1.8	<0.34
	-0.03	0.19 <sup>+0.07</sup> <sub>-0.05</sub>	<0.06	0.04 <sup>+0.02</sup> <sub>-0.01</sub>	5.6 <sup>+1.8</sup> <sub>-0.9</sub>	<0.31
	-0.06	0.12 <sup>+0.03</sup> <sub>-0.03</sub>	0.04 <sup>+0.01</sup> <sub>-0.01</sub>	0.024 <sup>+0.008</sup> <sub>-0.005</sub>	5.3 <sup>+1.2</sup> <sub>-0.8</sub>	0.35 <sup>+0.05</sup> <sub>-0.06</sub>
	-0.1	0.14 <sup>+0.07</sup> <sub>-0.04</sub>	0.05 <sup>+0.01</sup> <sub>-0.01</sub>	0.03 <sup>+0.01</sup> <sub>-0.01</sub>	4.7 <sup>+2.4</sup> <sub>-1.0</sub>	0.38 <sup>+0.07</sup> <sub>-0.13</sub>
$S\mu_{\text{SUMIRE}}^2$ <sup>c</sup>	Offset <sup>b,d</sup>	[CH <sub>2</sub> DOH]/[CH <sub>3</sub> OH]	[CHD <sub>2</sub> OH]/[CH <sub>3</sub> OH]	[CH <sub>3</sub> OD]/[CH <sub>3</sub> OH]	[CH <sub>2</sub> DOH]/[CH <sub>3</sub> OD]	[CHD <sub>2</sub> OH]/[CH <sub>2</sub> DOH]
	0.1	0.17 <sup>+0.03</sup> <sub>-0.03</sub>	0.03 <sup>+0.01</sup> <sub>-0.01</sub>	...	12 <sup>+3</sup> <sub>-3</sub>	0.18 <sup>+0.03</sup> <sub>-0.03</sub>
	0.06	0.13 <sup>+0.03</sup> <sub>-0.04</sub>	0.03 <sup>+0.01</sup> <sub>-0.01</sub>	...	5.5 <sup>+1.3</sup> <sub>-0.6</sub>	0.26 <sup>+0.03</sup> <sub>-0.04</sub>
	0.03	<0.40	<0.07	...	>11	0.17 <sup>+0.03</sup> <sub>-0.03</sub>
	0 <sup>e</sup>	>0.47	0.10 <sup>+0.04</sup> <sub>-0.04</sub>	...	>2.6	<0.21
	-0.03	0.28 <sup>+0.1</sup> <sub>-0.08</sub>	<0.05	...	8.0 <sup>+2.5</sup> <sub>-1.4</sub>	<0.19
	-0.06	0.19 <sup>+0.05</sup> <sub>-0.04</sub>	0.04 <sup>+0.01</sup> <sub>-0.01</sub>	...	7.9 <sup>+1.8</sup> <sub>-1.3</sub>	0.21 <sup>+0.03</sup> <sub>-0.04</sub>
	-0.1	0.21 <sup>+0.12</sup> <sub>-0.07</sub>	0.05 <sup>+0.01</sup> <sub>-0.01</sub>	...	7.2 <sup>+3.8</sup> <sub>-1.7</sub>	0.22 <sup>+0.05</sup> <sub>-0.07</sub>

#### Notes.

<sup>a</sup> For CH<sub>2</sub>DOH and CHD<sub>2</sub>OH, the abundances are derived by using the column densities calculated with the  $S\mu_{\text{JPL}}^2$  and  $S\mu_{\text{CDMS}}^2$  values, respectively.

<sup>b</sup> Offsets from the continuum peak position along the envelope (P.A. 5°).

<sup>c</sup> For CH<sub>2</sub>DOH and CHD<sub>2</sub>OH, the abundances are derived by using the column densities calculated with the  $S\mu_{\text{SUMIRE}}^2$  value.

<sup>d</sup> The abundance ratios are plotted in Figure 2.

<sup>e</sup> At the continuum peak, the observed column densities are seriously affected by the high optical depth of dust continuum emission, and hence, we focus on the abundances at the six positions in the envelope in this paper.

## 6. Distributions and Velocity Maps of the Disk/Envelope System

It is of fundamental importance for the characterization of this source to verify the protostellar mass and the presence/absence of the disk structure, which may relate to the evolutionary stage of the protostar. As mentioned in Section 2, various efforts toward this direction have been reported. In particular, Imai et al. (2019) studied velocity structures of the disk/envelope system with the CH<sub>3</sub>OH (12<sub>6,7</sub> – 13<sub>5,8</sub>, E,  $E_u = 360$  K) and HCOOH (12<sub>0,12</sub> – 11<sub>0,11</sub>,  $E_u = 83$  K) lines at a resolution of 0''1. Since the resolution of our data is higher by a factor of 3–4, we reinvestigate the kinematic structure of the disk/envelope system with these molecular species.

The upper panels of Figure 3 show the moment zero maps of CH<sub>3</sub>OH (18<sub>3,15</sub> – 18<sub>2,16</sub>, A,  $E_u = 447$  K) and HCOOH (12<sub>0,12</sub> – 11<sub>0,11</sub>), respectively. The velocity range for the integration is from  $-0.2$  km s<sup>-1</sup> to 14.5 km s<sup>-1</sup>, where the systemic velocity is 8.34 km s<sup>-1</sup> (Yen et al. 2015). The moment zero map of CH<sub>3</sub>OH is the same as that in Figure 1(a). We choose this line of CH<sub>3</sub>OH for the kinematic analysis in the next section because of the relatively high signal-to-noise ratio. In addition, we can avoid the contamination from the outflow as much as possible with the line, since it has the relatively high upper-state energy among the CH<sub>3</sub>OH lines in our observation. In the upper panel of Figure 3(b), the HCOOH line shows a more compact distribution, which would selectively trace the velocity structure of the inner disk/envelope system. To study the inner structure, we also explore the velocity structure of the HCOOH emission in this paper.

The lower panels of Figure 3 show the moment one maps of CH<sub>3</sub>OH and HCOOH, respectively, where the velocity range is from 1.6 km s<sup>-1</sup> to 13.3 km s<sup>-1</sup>. The velocity gradient can be seen in both of the moment one maps. The velocity gradient in

the map of CH<sub>3</sub>OH is almost along the west-to-east axis, whereas that of HCOOH is rather close to the south-to-north axis. The outflow and disk/envelope directions are suggested to be nearly along the west-to-east (P.A. 95°) and south-to-north axes (P.A. 5°), respectively (e.g., Bjerkeli 2023). Hence, the observed velocity structure has a gradient along the different directions from the suggested disk/envelope system, particularly for the CH<sub>3</sub>OH line. As Imai et al. (2019) and Oya et al. (2022) pointed out, this can occur for the contribution of the infalling-rotating motion, which will be discussed later (Section 7.1).

The moment zero maps of CH<sub>3</sub>OH and HCOOH show a ring-shaped distribution in spite of the almost edge-on configuration suggested by Bjerkeli et al. (2019) and Evans et al. (2023). The CH<sub>3</sub>OH distribution is more extended in height of the disk/envelope system than the HCOOH distribution as well as in radius. Part of the CH<sub>3</sub>OH emission can be caused by the interaction with the outflow as shown in the lower panel of Figure 3(b) in addition to the infalling-motion effect above and below the midplane of the disk/envelope system. Such a stratified molecular distribution was also reported in the other low-mass source: HH212 by Lee et al. (2022). The HCOOH emission would be less affected by the outflow interaction than the CH<sub>3</sub>OH emission and provide us with a better estimate of the disk height. Therefore, the apparent scale height of the disk/envelope system is roughly estimated to be about 20 au based on the HCOOH maps for the analysis in the next section (Figure 3(b)).

Moreover, in B335, the SiO emission was reported to have an extended distribution along the east-to-west axis near the protostar ( $< 0''1$ ) by Bjerkeli et al. (2019). SiO is well known as a shock tracer (e.g., Mikami et al. 1992; Bachiller & Pérez Gutiérrez 1997), and could trace the launching point of the outflow or the accretion shock of infalling material

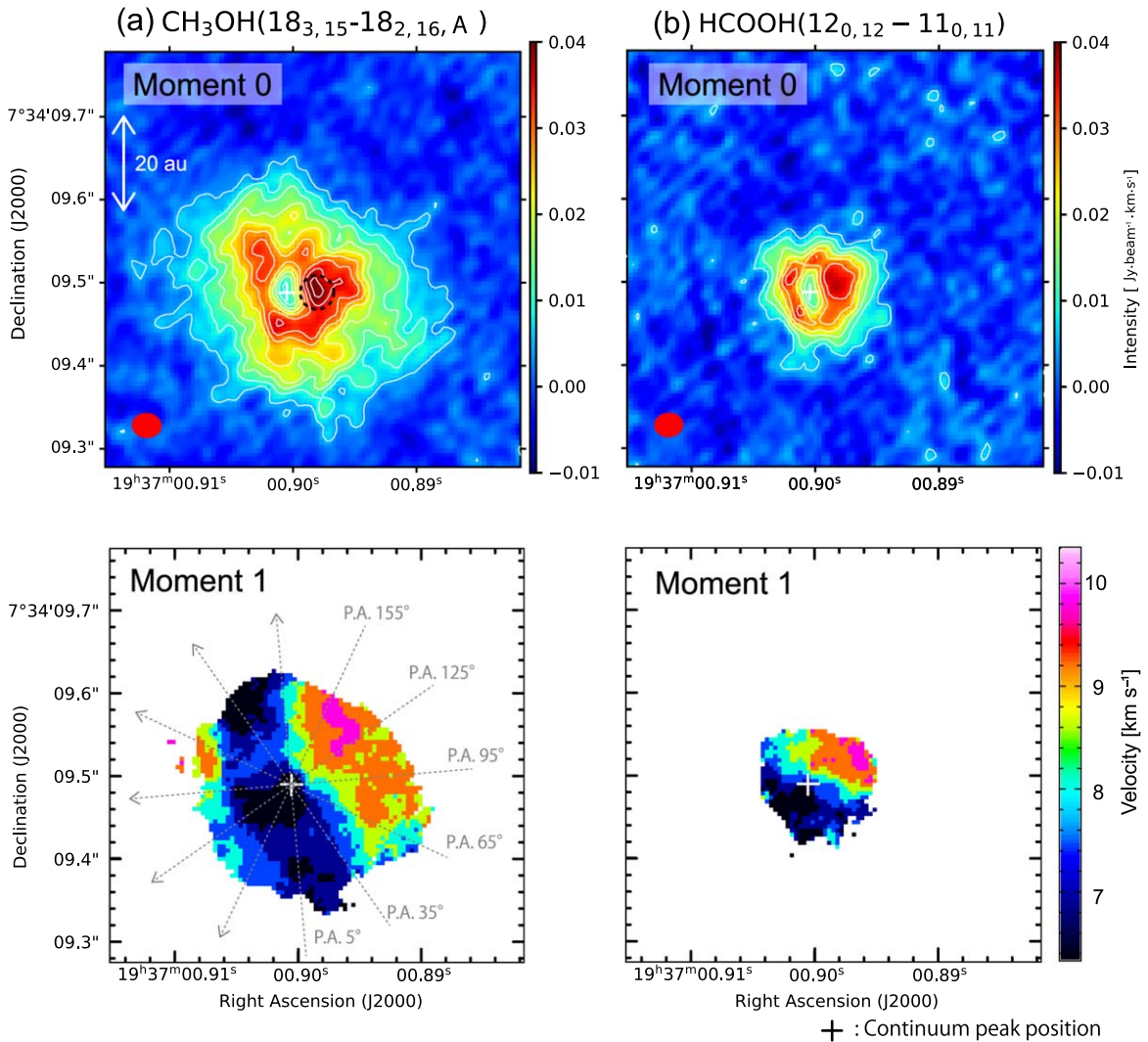


**Figure 3.** (a), (b) Moment zero and one maps of the  $\text{CH}_3\text{OH}$  ( $18_{3,15} - 18_{2,16}$ , A) and  $\text{HCOOH}$  ( $12_{0,12} - 11_{0,11}$ ) emission in the upper and lower panels, respectively. The moment zero map of  $\text{CH}_3\text{OH}$  is the same as Figure 1(a), where the black dotted circle indicates the area covered by the SiO emission with previous work, as mentioned in Section 6. Contour levels for  $\text{HCOOH}$  are every  $3\sigma$  from  $3\sigma$ , where  $\sigma$  is  $1.8 \text{ mJy beam}^{-1}$ . For the moment zero and one maps, the integrated velocity range is from  $-0.2 \text{ km s}^{-1}$  to  $14.5 \text{ km s}^{-1}$  and from  $1.6 \text{ km s}^{-1}$  to  $13.3 \text{ km s}^{-1}$ , respectively. The systemic velocity is  $8.34 \text{ km s}^{-1}$  (Yen et al. 2015). The gray dotted arrows in the moment one map of  $\text{CH}_3\text{OH}$  show the directions of the PV diagrams of Figures 4, 6, and 7. The white cross marks represent the continuum peak ( $\alpha_{2000}, \delta_{2000}$ ) =  $(19^{\text{h}}37^{\text{m}}00^{\text{s}}.90, +7^{\circ}34'09''.49)$ . The red ellipses represent the beam size.

(Imai et al. 2019). Its distribution covers the area where both the  $\text{CH}_3\text{OH}$  and  $\text{HCOOH}$  line intensities are enhanced around the west of the protostar, as shown in the dotted black circle of Figure 3(a). In terms of the detection of SiO, the intensity enhancement would be caused by a shock on the surface area of the disk/envelope system rather than protostellar heating.

## 7. Kinematics of the Disk/Envelope System with FERIA

In this section, we analyze the  $\text{CH}_3\text{OH}$  and  $\text{HCOOH}$  data to determine the protostellar mass ( $M_{\text{star}}$ ), the centrifugal barrier ( $r_{\text{CB}}$ ), and the inclination ( $i$ ) of the disk/envelope system, the inner radius ( $R_{\text{in}}$ ) with the aid of a general-purpose computer code FERIA (Flat Envelope model with Rotation and Infall under Angular momentum conservation) developed by Oya et al. (2022). The physical meaning of  $R_{\text{in}}$  depends on the model, and hence, we will specify it for each case later. We perform the  $\chi^2$  test to obtain the best-fit model parameters on the molecular-line data cube, where the intensities are higher than  $3\sigma$  noise level;  $1.5 \text{ mJy beam}^{-1}$  and  $1.8 \text{ mJy beam}^{-1}$  for

$\text{CH}_3\text{OH}$  and  $\text{HCOOH}$ . For the models, we set the height of the disk/envelope system to be 20 au based on the apparent height in the map of  $\text{HCOOH}$ , as mentioned in Section 6.

### 7.1. $\text{CH}_3\text{OH}$ ( $18_{3,15} - 18_{2,16}$ , A)

Based on the distributions in the moment zero and one maps (Figure 3(a)) and the analyses presented by Imai et al. (2019), the  $\text{CH}_3\text{OH}$  emission is expected to trace an IRE. To explore the velocity structure of the  $\text{CH}_3\text{OH}$  ( $18_{3,15} - 18_{2,16}$ , A) emission, we prepare the IRE models by taking  $M_{\text{star}}$ ,  $r_{\text{CB}}$ , and  $i$  as the free parameters.  $R_{\text{in}}$  here represents the inner radius of IRE ( $R_{\text{in}}$ ) traced by the  $\text{CH}_3\text{OH}$  emission, which is assumed to be equal to  $r_{\text{CB}}$ .  $R_{\text{out}}$  indicates the outer radius of IRE ( $R_{\text{out}}$ ) traced by the  $\text{CH}_3\text{OH}$  emission, which is fixed to be 24 au according to the observed emission. The parameter ranges are summarized in Table 4.

The disk/envelope system was suggested to be the almost edge-on configuration ( $0^\circ$  for face-on: e.g., Bjerkeli et al. 2019; Imai et al. 2019; Evans et al. 2023), and hence, we set the range

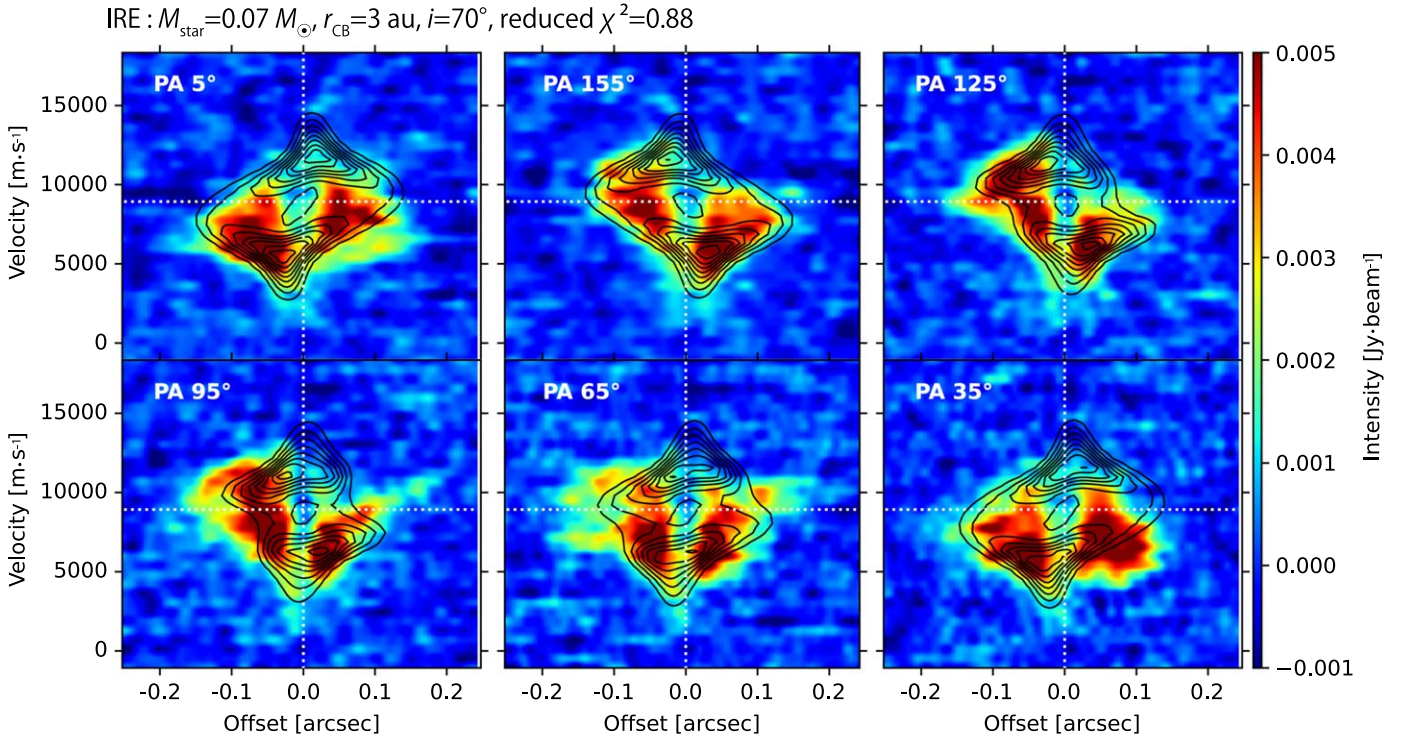


**Figure 4.** PV diagrams of  $\text{CH}_3\text{OH}$  ( $18_{3,15} - 18_{2,16}$ , A) in colors and the best-fit model obtained by the  $\chi^2$  analysis for the IRE model with FERIA in contours. The best-fit parameters for the IRE model are the protostellar mass of  $0.07M_{\odot}$ , the outer radius of 24 au, the inner radius and the centrifugal barrier of 3 au, and the inclination of  $70^{\circ}$  ( $90^{\circ}$  for edge-on), where the reduced  $\chi^2$  value is 0.88. Dotted horizontal lines show the systemic velocity of  $8.34 \text{ km s}^{-1}$  (Yen et al. 2015), and dotted vertical lines show the protostar position.

**Table 4**  
Free Parameters in the Reduced  $\chi^2$  Test on the Cube Data

Model	Molecule	$M_{\text{star}}$ ( $M_{\odot}$ )	$r_{\text{CB}}$ (au)	$i$ (deg)	$R_{\text{in}}$ (au)	$R_{\text{out}}$ (au)	Reduced $\chi^2$ Values
IRE (Best-fit)	$\text{CH}_3\text{OH}$	0.02–0.08 0.07	2–9 3	70–90 70	$r_{\text{CB}}$	24	0.88
IRE (Best-fit)	$\text{HCOOH}$	0.02–0.08 0.04	2–9 7	70–90 90	$r_{\text{CB}}$	10	0.81
Combined (Best-fit)	$\text{HCOOH}$	0.02–0.08 0.03	2–9 6	70–90 90	1	10	0.82
Kepler (Best-fit)	$\text{HCOOH}$	0.02–0.08 0.05	10	70–90 90	1–6 5	$r_{\text{CB}}$	0.82

**Notes.** In the FERIA code, the heights of the envelope and disk are set to be 20 au. The fittings are applied for the cube data of  $\text{CH}_3\text{OH}$  and  $\text{HCOOH}$  with the intensities higher than  $3\sigma$  noise level;  $1.5 \text{ mJy beam}^{-1}$  and  $1.8 \text{ mJy beam}^{-1}$ , respectively.

from  $70^{\circ}$  to  $90^{\circ}$  for  $i$ . The position angles (P.A.) of the disk/envelope are set to be  $5^{\circ}$  (Bjerkeli et al. 2019; Cabedo et al. 2021; Bjerkeli 2023). We compare the model with the observation on the cube data to calculate the reduced  $\chi^2$  value. Then, we obtain the best-fit parameters at the reduced  $\chi^2$  values of 0.88, where  $M_{\text{star}}$ ,  $r_{\text{CB}} (= R_{\text{in}})$ , and  $i$  are  $0.07M_{\odot}$ , 3 au, and  $70^{\circ}$ , respectively.

Imai et al. (2019) reported  $M_{\text{star}}$  of  $0.03\text{--}0.1 M_{\odot}$  and  $r_{\text{CB}} < 8 \text{ au}$ . With the same data, Oya et al. (2022) obtained the best-fit parameters of  $M_{\text{star}} = 0.03 M_{\odot}$  and  $r_{\text{CB}} = 2 \text{ au}$  through the  $\chi^2$  tests (the reduced  $\chi^2$  value = 0.77) for the infalling-rotating model. They also analyzed the observed data with a Keplerian model, resulting in the best-fit parameters of  $M_{\text{star}} = 0.07 M_{\odot}$  and  $R_{\text{in}} = 2 \text{ au}$  at a reduced  $\chi^2$  value of 0.78. Bjerkeli et al. (2019) independently derived  $M_{\text{star}}$  to be  $0.08 M_{\odot}$  from the analysis of the position–velocity (PV)

diagrams of  $\text{CH}_3\text{OH}$  and  $\text{SO}_2$  at a similar resolution to our observation, assuming a Keplerian rotation. Thus, the small  $M_{\text{star}}$  and  $r_{\text{CB}}$  values obtained in this study are consistent with those reported in the previous works.

Figure 4 shows the PV diagrams of the best-fit model in contours compared with those of  $\text{CH}_3\text{OH}$  in colors, where the cutting width is 7 au for PVs. Directions of the PV diagrams are shown as the arrows in Figure 3(a). The model can almost reproduce the major features of the observation, although some emission is veiled by the dust continuum at the continuum peak (offset of  $0''0$ ). In addition, the redshifted component is weaker than the blueshifted one in Figure 4. This may be due to the self-absorption in the infalling gas (i.e., inverse P-Cygni profile). An increase in the velocity around the offsets of  $0''1\text{--}0''2$ , as seen in the panels of P.A.  $95^{\circ}$  and  $65^{\circ}$ , is likely a contribution of an outflow interaction.

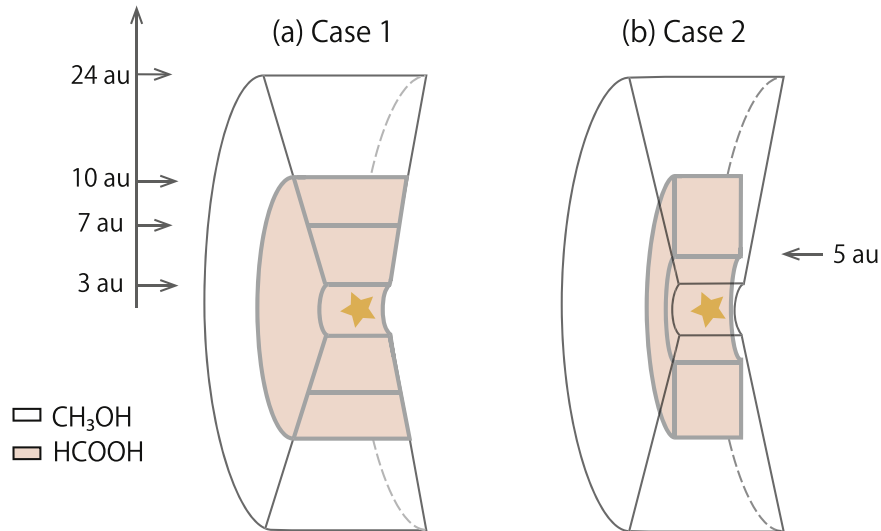


**Figure 5.** Schematic illustration of the disk/envelope system of B335. The HCOOH and CH<sub>3</sub>OH emitting region areas are enclosed by colors and by solid and dashed lines, respectively. (a) Inner envelope traced by the HCOOH emission and overall envelope traced by the CH<sub>3</sub>OH emission. (b) A stratified molecular distribution is considered. A possible Keplerian disk is traced by the HCOOH emission and the infalling gas envelope is traced by the CH<sub>3</sub>OH emission motion.

## 7.2. HCOOH ( $12_{0,12} - 11_{0,11}$ )

We obtain  $r_{\text{CB}}$  of 3 au in the analysis for the CH<sub>3</sub>OH line. This means that if there were a rotationally supported disk inside the infalling-rotating envelope traced by CH<sub>3</sub>OH, its radius would be 3 au. This size cannot fully be resolved by the resolution of our data ( $\sim 5$  au). Since the HCOOH emission has a distribution of 10 au in radius that is larger than the obtained  $r_{\text{CB}}$ , it seems to overlap with part of the CH<sub>3</sub>OH distribution. As well, the moment one map (Figure 3(b)) looks similar to the infalling-rotating motion (Oya et al. 2022). Nevertheless, we examine the following two cases to explore the velocity structure by using the model on the cube data. One is the case that HCOOH traces an infalling-rotating motion with  $R_{\text{out}}$  of 10 au in the inner part of the disk/envelope system. In this case, there could be a very small rotationally supported disk within  $R_{\text{in}}$  ( $r_{\text{CB}}$ ). Another case is that a Keplerian disk with a radius of 10 au ( $= R_{\text{out}} = r_{\text{CB}}$ ) is traced by HCOOH, where the gas infalling on the above and below disk midplane toward the protostar is traced by CH<sub>3</sub>OH. The two cases are schematically shown in Figure 5. In the following cases of Sections 7.2.1 and 7.2.2,  $R_{\text{out}}$  and  $R_{\text{in}}$  refer to the outer and inner radii of the structure traced by the HCOOH emission, respectively.

### 7.2.1. Case 1: IRE

We here consider the IRE model with  $R_{\text{out}}$  of 10 au as well as the combined model. In the combined model, the IRE model and the Keplerian rotation model are considered simultaneously, where the Keplerian disk is assumed to exist inward of the centrifugal barrier of the IRE (i.e., for  $r_{\text{Kepler}} < r_{\text{CB}}$ ). At first, we prepare the IRE models using  $M_{\text{star}}$ ,  $r_{\text{CB}} (= R_{\text{in}})$ , and  $i$  summarized in Table 4, and perform a reduced  $\chi^2$  test for HCOOH on the cube data. The best-fit value of  $M_{\text{star}}$  is  $0.04 M_{\odot}$ , where the reduced  $\chi^2$  value is 0.81. The other best-fit parameters are:  $r_{\text{CB}} (= R_{\text{in}}) = 7$  au, and  $i = 90^\circ$ . These parameters are slightly different from those in the CH<sub>3</sub>OH analysis (Section 7.1).  $r_{\text{CB}}$  of 7 au is within the range reported by Imai et al. (2019). The larger value of  $r_{\text{CB}}$  than that obtained by the CH<sub>3</sub>OH analysis ( $r_{\text{CB}} = 3$  au) may be caused by the weaker intensities near the continuum peak. In Figure 6, PV diagrams

of the best-fit IRE (upper) and Combined (below) models are overlaid on those of the HCOOH emission. Most of the observed features are reproduced by the IRE model. If we set  $r_{\text{CB}} (= R_{\text{in}})$  to be 3 au obtained in the CH<sub>3</sub>OH analysis, the best-fit parameters of  $M_{\text{star}}$  and  $i$  are  $0.03 M_{\odot}$  and  $90^\circ$ , respectively, where the reduced  $\chi^2$  value is 0.84.

For the combined models, we fix the inner radius ( $R_{\text{in}}$ ) of the Keplerian part to be 1 au to reduce the number of free parameters. The outer radius ( $R_{\text{out}}$ ) and the ranges for the other parameters ( $M_{\text{star}}$ ,  $r_{\text{CB}}$ , and  $i$ ) are the same as those of the IRE model. The  $\chi^2$  analysis on the data cube yields the best-fit parameters as:  $M_{\text{star}} = 0.03 M_{\odot}$ ,  $r_{\text{CB}} (= R_{\text{in}}) = 6$  au, and  $i = 90^\circ$ , where the reduced  $\chi^2$  value is 0.82. Then, we cannot confirm the disk structure in this observation, because of the insufficient resolution and the relatively weak emission of the central part due to the dust opacity effect.

### 7.2.2. Case 2: Keplerian Rotation

The stratified molecular distributions mentioned above being considered, the disk structure could be embedded in the infalling gas traced by the CH<sub>3</sub>OH emission. An infalling-rotating motion on the surface of the disk/envelope system near the protostar would be traced by CH<sub>3</sub>OH (Figure 5(b)). In this case, HCOOH might trace a Keplerian disk with a radius of 10 au. With this situation in mind, we prepare the models with a Keplerian motion in the FERIA code. The size of the disk,  $R_{\text{out}}$ , is fixed to be 10 au, and the free parameters are  $M_{\text{star}}$ ,  $R_{\text{in}}$ , and  $i$ , which are varied in the ranges of  $0.02$ – $0.08 M_{\odot}$ ,  $1$ – $6$  au, and  $70$ – $90^\circ$ , respectively, as summarized in Table 4. We obtain the best-fit parameters of  $M_{\text{star}} = 0.05 M_{\odot}$ ,  $R_{\text{in}} = 5$  au, and  $i = 90^\circ$  with the reduced  $\chi^2$  value of 0.82.  $i$  suggests a completely edge-on disk, while  $M_{\text{star}}$  is similar to that in the CH<sub>3</sub>OH analysis based on the IRE model. Figure 7 shows PV diagrams of the best-fit Keplerian models overlaid on those of the HCOOH emission. The reduced  $\chi^2$  value in Case 2 is similar to that in Case 1.

In short, our observation is not able to determine which of Case 1 and Case 2 is more appropriate for the HCOOH distribution. Nevertheless, we can conclude that B335 has a very small protostellar mass and a disk structure smaller than the HCOOH emission. Our analysis of the HCOOH emission

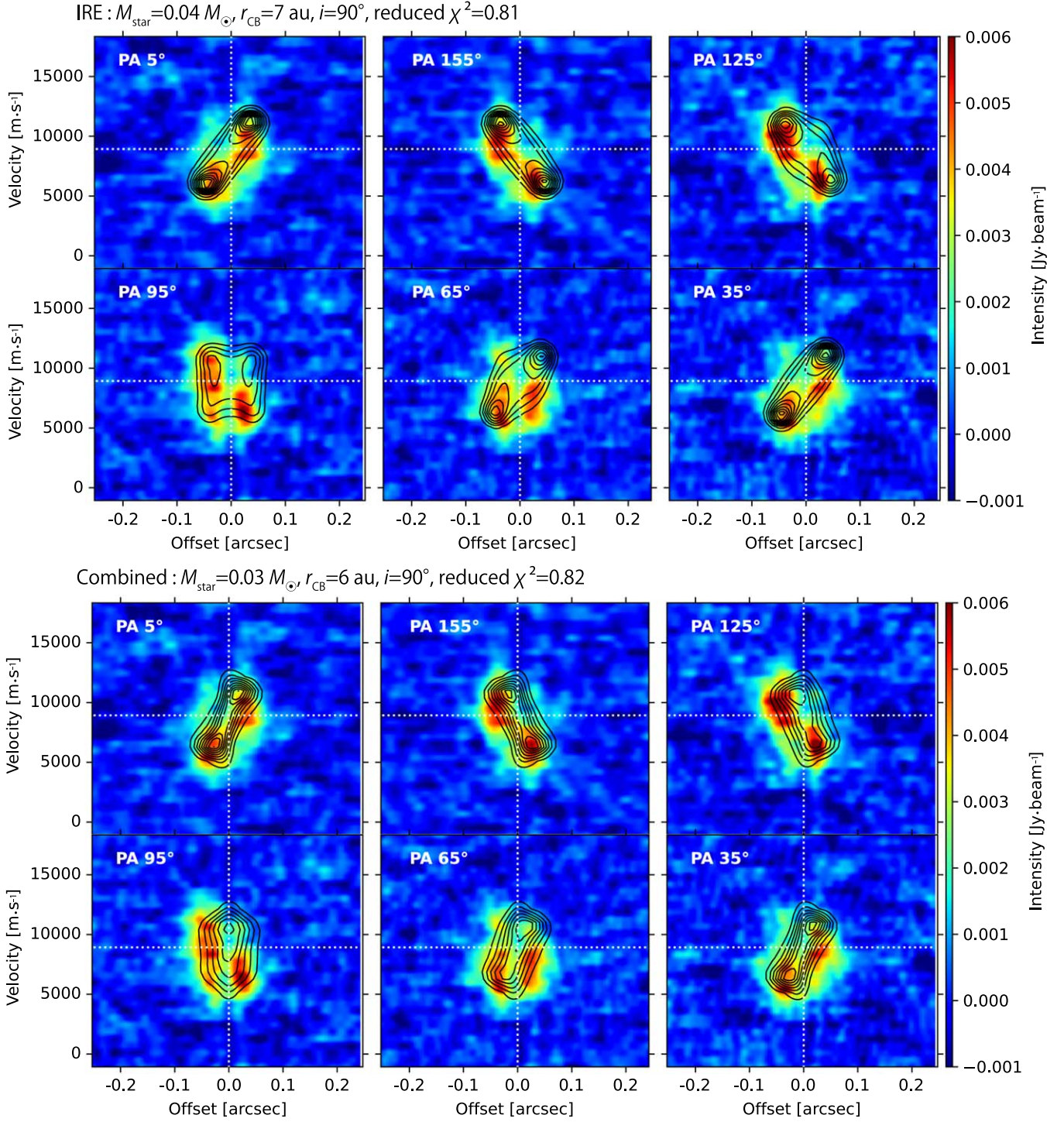


**Figure 6.** PV diagrams of HCOOH ( $12_{0,12} - 11_{0,11}$ ) in colors and the best-fit model obtained by the  $\chi^2$  analysis for the IRE model (upper) and the combined model (lower) with FERIA in contours. The parameters for the IRE model are the protostellar mass of  $0.04M_{\odot}$ , the outer radius of 10 au, the inner radius and the centrifugal barrier of 7 au, and the inclination of  $90^{\circ}$  ( $90^{\circ}$  for edge-on), where the reduced  $\chi^2$  value is 0.81. Those for the combined model are the protostellar mass of  $0.03M_{\odot}$ , the outer radius of 10 au, the inner radius and the centrifugal barrier of 6 au, and the inclination of  $90^{\circ}$  ( $90^{\circ}$  for edge-on), where the reduced  $\chi^2$  value is 0.82. Dotted horizontal lines show the systemic velocity of  $8.34 \text{ km s}^{-1}$  (Yen et al. 2015), and dotted vertical lines show the protostar position.

suggests that we need a higher-angular resolution and/or other molecular lines specifically tracing a more compact distribution to find a Keplerian disk.

## 8. Deuteration and Physical Environment

Based on our analysis in Section 7, the  $\text{CH}_3\text{OH}$  emission traces an infalling-rotating motion within 24 au in radius. The freefall

time is very short, which is roughly estimated to be only  $\sim 10$  yr, where the infall velocity of  $5 \text{ km s}^{-1}$  is assumed at the radius of 10 au. Even if the dynamical timescale is estimated by the Kepler time, it is about 100 yr. As a result, there would not be enough time to change the isotopic ratios in the inner envelope by gas-phase chemical reactions. Furthermore, our analysis with FERIA implies a tiny disk structure with a radius of  $< 7$  au ( $r_{\text{CB}}$ ). Considering these results, we here discuss the abundance

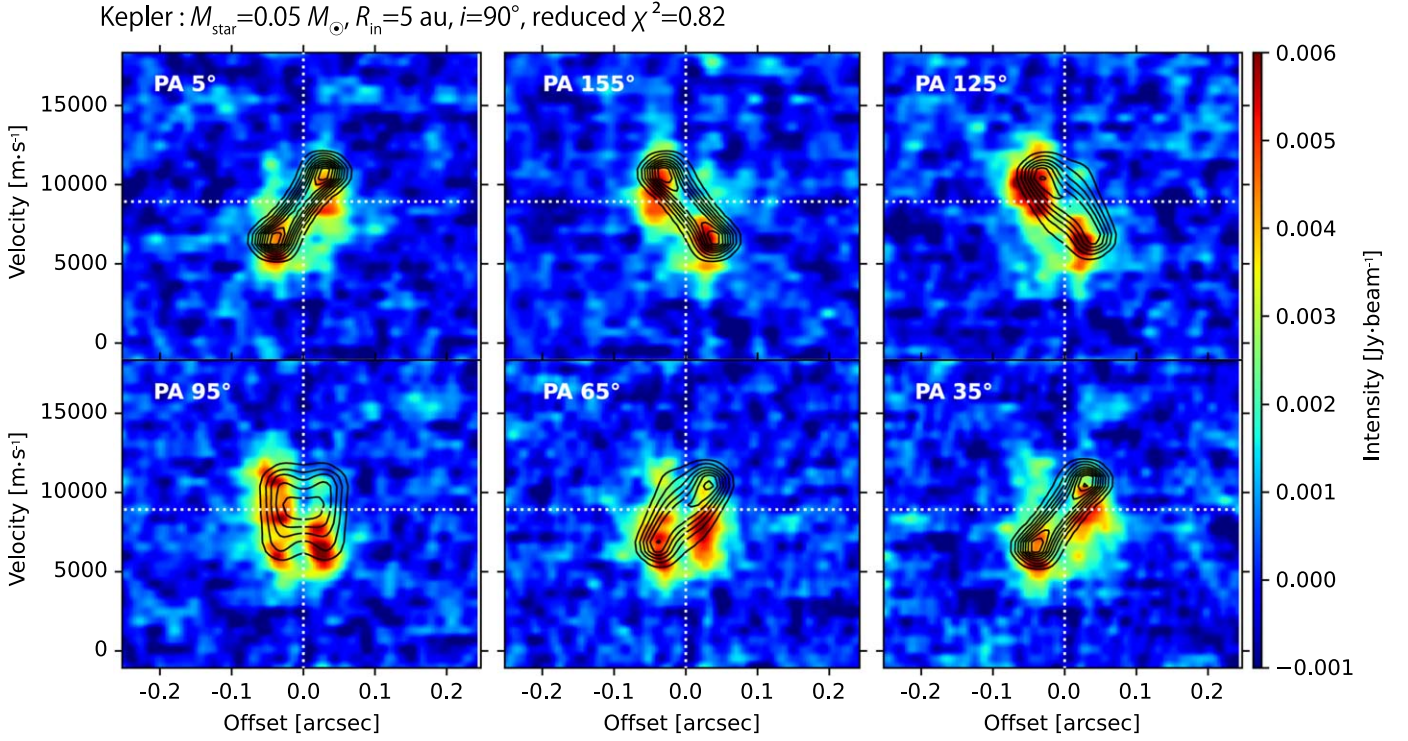


**Figure 7.** PV diagrams of HCOOH ( $12_{0,12} - 11_{0,11}$ ) in colors and the best-fit model obtained by the  $\chi^2$  analysis for the Keplerian disk model with FERIA in contours. The parameters for the model are the protostellar mass of  $0.05M_{\odot}$ , the inner radius of 5 au, the outer radius of 10 au, and the inclination of  $90^{\circ}$  ( $90^{\circ}$  for edge-on), where the reduced  $\chi^2$  value is 0.82. Dotted horizontal lines show the systemic velocity of  $8.34 \text{ km s}^{-1}$  (Yen et al. 2015), and dotted vertical lines show the protostar position.

ratios  $[\text{CH}_2\text{DOH}]/[\text{CH}_3\text{OH}]$ ,  $[\text{CHD}_2\text{OH}]/[\text{CH}_2\text{DOH}]$ , and  $[\text{CH}_2\text{DOH}]/[\text{CH}_3\text{OD}]$  in B335 and compare them with those in other sources reported previously.

### 8.1. $[\text{CH}_2\text{DOH}]/[\text{CH}_3\text{OH}]$

The  $[\text{CH}_2\text{DOH}]/[\text{CH}_3\text{OH}]$  ratio can be converted to the D/H ratio by dividing by 3 because there are three equivalent H atoms of the methyl group for the D substitution. The D/H ratio was reported to be up to 0.1 toward low-mass protostars (e.g., Taquet et al. 2019; van Gelder et al. 2020, 2022). van Gelder et al. (2022) discussed the D/H ratio of  $[\text{CH}_2\text{DOH}]/[\text{CH}_3\text{OH}]$  among large samples including low-mass and intermediate sources as well as high-mass sources, where the lines of  $\text{CH}_3\text{OH}$  isotopologues,  $^{13}\text{CH}_3\text{OH}$  and  $\text{CH}_3^{18}\text{OH}$ , as well as normal  $\text{CH}_3\text{OH}$  lines are used. Since most of the samples of low-mass protostars in their paper have a ratio much lower than 0.1, its average in low-mass protostars was reported to be  $[\text{CH}_2\text{DOH}]/[\text{CH}_3\text{OH}] \sim 0.06$  (D/H  $\sim 0.02$ ). It is higher than the ratios in high-mass protostars. The  $[\text{CH}_2\text{DOH}]/[\text{CH}_3\text{OH}]$  ratio in B335 is  $[0.09\text{--}0.38]$  (D/H  $\sim [0.03\text{--}0.13]$ ), which tends to be relatively high even among other low-mass protostars and low-mass prestellar cores (D/H  $\sim 0.034 \pm 0.019$ ; van Gelder et al. 2022). This result may be related to the young evolutionary stage of the B335 protostar. Since not enough time would have passed to decrease the D/H ratio to its equilibrium ratio at the current temperature in B335, the D/H ratio in the prestellar stage may be converted to some extent. Nevertheless, the derived D/H ratio could be due to underestimating the column density of  $\text{CH}_3\text{OH}$ . The optical depths of the  $\text{CH}_3\text{OH}$  lines are derived to be relatively high, as summarized in Appendix D. The D/H ratio of  $\text{CH}_3\text{OH}$  could thus be consistent with those of the previous reports. Anyway,

further confirmation of the D/H ratio by optically thin isotopologues is awaited: a few  $^{13}\text{CH}_3\text{OH}$  lines are in the observed spectral windows, but none of them provide further constraints on the column density.

Note that the  $S\mu_{\text{JPL}}^2$  values are used for  $\text{CH}_2\text{DOH}$  in the previous studies. Even if we employed the  $S\mu_{\text{JPL}}^2$  values in our calculation, the D/H ratio in B335 would be smaller only by a factor of  $\sim 1.5$ . Therefore, the above trend on  $[\text{CH}_2\text{DOH}]/[\text{CH}_3\text{OH}]$  does not change even for this case (Table 3).

### 8.2. $[\text{CHD}_2\text{OH}]/[\text{CH}_2\text{DOH}]$

The  $[\text{CHD}_2\text{OH}]/[\text{CH}_2\text{DOH}]$  ratio (D/H ratio) of  $[0.14\text{--}0.29]$  in B335 is comparable to those in the low-mass protostellar sources IRAS 16293–2422 Source A ( $0.20 \pm 0.07$ ) and B ( $0.25 \pm 0.09$ ; Drozdovskaya et al. 2022). For the low-mass protostellar sources, B1-c and Serpens S68N, van Gelder et al. (2022) derived the ratios  $0.13 \pm 0.02$  and  $0.12 \pm 0.05$ , respectively, on the assumption of the temperature of 150 K. They are slightly lower than or comparable to our result. On the other hand, our result in B335 is lower than the ratios in the other low-mass protostellar sources, NGC1333 IRAS 2A ( $0.70 \pm 0.26$ ), IRAS 4A ( $0.56 \pm 0.22$ ; Taquet et al. 2019), and HOPS373SW ( $0.75$ ; Lee et al. 2023). Recently, the  $\text{CHD}_2\text{OH}$  and  $\text{CH}_2\text{DOH}$  lines were detected in the prestellar sources as well, the ratios being  $0.8 \pm 0.4$  in H-MM1 and  $0.5 \pm 0.3$  in L694-2 (Lin et al. 2023). Furthermore, the D/H ratio from  $\text{CHD}_2\text{OH}$  and  $\text{CH}_2\text{DOH}$  is reported to be higher than that from  $\text{CH}_2\text{DOH}$  and  $\text{CH}_3\text{OH}$  in the above protostellar and prestellar sources (Appendix E). Our results in B335 follow this trend even in the close vicinity of protostar ( $< 24 \text{ au}$ ). Note that the upper range of the D/H ratio of  $\text{CH}_3\text{OH}$  is comparable to the lower range of the  $[\text{CHD}_2\text{OH}]/$

[CH<sub>2</sub>DOH] ratio. There may be an effect of the underestimated CH<sub>3</sub>OH column density due to the high optical depth in our observation. Since the actual CH<sub>3</sub>OH column density could be higher, the [CH<sub>2</sub>DOH]/[CH<sub>3</sub>OH] ratio would be lower, resulting in the values in the range of D/H ratio from CHD<sub>2</sub>OH and CH<sub>2</sub>DOH higher than that from CH<sub>2</sub>DOH and CH<sub>3</sub>OH.

### 8.3. [CH<sub>2</sub>DOH]/[CH<sub>3</sub>OD]

The [CH<sub>2</sub>DOH]/[CH<sub>3</sub>OD] ratio in B335 is found to be as high as [4.9–15] (Table 3). Similar values were found in other low-mass sources (e.g., Parise et al. 2004, 2006; Bizzocchi et al. 2014; Jørgensen et al. 2018). In the low-mass Class 0 protostellar source, IRAS 16293-2422 Source B, the ratio is derived to be 3.9 at the position shifted from the continuum peak as one beam to avoid the dust opacity effects with ALMA (Jørgensen et al. 2018). Bizzocchi et al. (2014) reported its lower limit of 10 in the external layers of the prestellar core L1544. On the other hand, the ratios in some high-mass star-forming regions are lower than 1.0 (e.g., Jacq et al. 1993; Ratajczak et al. 2011; Belloche et al. 2016; Bøgelund et al. 2018; Wilkins & Blake 2022). Thus, it is recognized that there is a systematic trend between low-mass and high-mass protostars. The physical environment would thus be one of the important effects on the [CH<sub>2</sub>DOH]/[CH<sub>3</sub>OD] ratio.

Even if the  $S\mu^2_{\text{SUMIRE}}$  values for CH<sub>2</sub>DOH were used for the calculation in the previously reported [CH<sub>2</sub>DOH]/[CH<sub>3</sub>OD] ratios, the trend would still be significant for most cases. For the strong lines of CH<sub>2</sub>DOH, except for some c-type transitions or extremely high excitation ones, the differences in  $S\mu^2$  between the JPL database and the experiment are within a factor of a few. It is therefore hard to explain the reported difference of the [CH<sub>2</sub>DOH]/[CH<sub>3</sub>OD] ratios more than an order of magnitude only by the different  $S\mu^2$  values used in each study.

For CH<sub>3</sub>OH, the methyl group has three equivalent H atoms, while the hydroxy group has only one H atom. If the hydrogenation of CO randomly occurs without isotope effect, the [CH<sub>2</sub>DOH]/[CH<sub>3</sub>OD] ratio should be 3. This is so-called the statistical ratio, which is predicted by conventional gas-grain chemical models (e.g., Charnley et al. 1997; Osamura et al. 2004). However, it is known that the deuterium fractionation of the CH<sub>3</sub> group can be enhanced through the abstraction of H by the D atom and the subsequent addition of D on the grain surface (Hidaka et al. 2009). This additional process occurs efficiently if the atomic D/H ratio on dust grains is high in cold conditions. This mechanism would make the [CH<sub>2</sub>DOH]/[CH<sub>3</sub>OD] ratio higher than the statistical ratio of 3. Such a high abundance ratio was also suggested with chemical models by Kulterer et al. (2022). According to their studies, CH<sub>3</sub>OD is formed at a warm-up stage, although CH<sub>2</sub>DOH could be inherited from the prestellar stage to the protostellar stage.

The chemical pathway for CH<sub>3</sub>OD is still controversial, and many studies have been done by the chemical models (e.g., Charnley et al. 1997; Rodgers & Charnley 2002; Osamura et al. 2004; Taquet et al. 2014; Kulterer et al. 2022; Wilkins & Blake 2022) and the laboratory experiments (e.g., Nagaoka et al. 2005; Ratajczak et al. 2009). Bøgelund et al. (2018) and Taquet et al. (2019) compared the [CH<sub>2</sub>DOH]/[CH<sub>3</sub>OD] ratios in high-mass sources (NGC 6334 I: 0.1-0.5) and low-mass sources (IRAS 2A: 0.8-3.6 and IRAS 4A: 1.2-5.3) with the

chemical models presented by Taquet et al. (2012, 2013, 2014). The models follow the deuteration of CH<sub>3</sub>OH in cold dense cores (10–40 K), resulting in a ratio close to or a little higher than 3. Hence, the observed trend for the high-mass protostellar source, NGC6334I, is not reproduced. On the other hand, Faure et al. (2015) reported a model that can reproduce the observational trend of the high and low [CH<sub>2</sub>DOH]/[CH<sub>3</sub>OD] ratios in low-mass and high-mass protostellar sources, respectively, considering the pathway exchanging between water and CH<sub>3</sub>OH in icy mantles of dust grains. Kulterer et al. (2022) also pointed out the same mechanism.

Recently, Wilkins & Blake (2022) discussed rapid D–H exchange in methanol-containing ices depending on the temperature, based on its chemical model and the observation of the high-mass star-forming region Orion KL. According to their observation, the column density of CH<sub>3</sub>OD starts to rise steeply at  $\sim 110$  K and keeps increasing until before  $\sim 185$  K. This result is consistent with their chemical model representing the rapid variation in the gas-phase CH<sub>3</sub>OD column density due to the D–H exchange between water and CH<sub>3</sub>OH on ices. In fact, the similar increase in the CH<sub>3</sub>OD column density as increasing temperature up to around 200 K is also supported experimentally (Souda et al. 2003; Kawanowa et al. 2004). Wilkins & Blake (2022) suggested that the low [CH<sub>2</sub>DOH]/[CH<sub>3</sub>OD] ratio in Orion KL is caused by the increase in the CH<sub>3</sub>OD column density at the temperature ( $\sim 100$ – $200$  K), while understanding the D–H exchange to produce CH<sub>3</sub>OD at a temperature higher than  $\sim 200$  K is controversial.

If the high temperature were the only key factor for increasing CH<sub>3</sub>OD (i.e., low [CH<sub>2</sub>DOH]/[CH<sub>3</sub>OD] ratio), the [CH<sub>2</sub>DOH]/[CH<sub>3</sub>OD] ratio in the inner envelope of B335 should be as low as in high-mass star-forming regions because of the high-temperature condition (107–217 K for CH<sub>3</sub>OH). However, this simple thought contradicts our observational result. Therefore, the ratio may also depend on the physical environment at the prestellar core phase. The timescale that the D–H exchange reaches a steady state in Orion KL is suggested to be  $< 10^3$  yr (Faure et al. 2015). The freefall and dynamical timescales in B335 on a few 10 au scale seems to be shorter than the chemical reaction timescale. Alternatively, there might be an effect of high cosmic rays in the envelope of B335, where the cosmic-ray ionization rate is reported to be  $10^{-16}$ – $10^{-14}$  s<sup>-1</sup> by Cabedo et al. (2021). This rate is higher than usually assumed in chemical models ( $10^{-17}$  s<sup>-1</sup>; Yamamoto 2017). Apparently, we need more observations of other protostellar sources in various physical environments to clarify the link between [CH<sub>2</sub>DOH]/[CH<sub>3</sub>OD] and the physical environment.

## 9. Summary

We study the CH<sub>3</sub>OH and its deuterated species in terms of the abundance ratios and kinematics of the disk/envelope system in the low-mass protostellar source B335 at a high resolution (0.''03 $\sim$ 5 au) with ALMA. The main results are summarized below.

1. We analyze four lines of CH<sub>2</sub>DOH, three lines of CHD<sub>2</sub>OH, and one line of CH<sub>3</sub>OD as well as six lines of CH<sub>3</sub>OH in Band 6 originally observed by Okoda et al. (2022). The CHD<sub>2</sub>OH (4<sub>1,2</sub>–4<sub>0,1</sub>, o<sub>1</sub>–e<sub>0</sub>) line emission is newly identified in this paper, which was previously unidentified by Okoda et al. (2022). These molecular lines are ring-shaped and extended within 24 au in radius around the protostar.

2. The five abundance ratios ( $[\text{CH}_2\text{DOH}]/[\text{CH}_3\text{OH}]$ ,  $[\text{CHD}_2\text{OH}]/[\text{CH}_3\text{OH}]$ ,  $[\text{CH}_3\text{OD}]/[\text{CH}_3\text{OH}]$ ,  $[\text{CH}_2\text{DOH}]/[\text{CH}_3\text{OD}]$ , and  $[\text{CHD}_2\text{OH}]/[\text{CH}_2\text{DOH}]$ ) are almost constant over the envelope. This likely originates from the short dynamical timescale (10–100 yr) in the inner envelope compared to the chemical timescale ( $\sim 10^4$  yr).

3. We examine the effect of  $S\mu^2$  values on the calculation for column densities and temperatures of  $\text{CH}_2\text{DOH}$  and  $\text{CHD}_2\text{OH}$ , because the calculated  $S\mu^2$  values ( $S\mu^2_{\text{JPL}}$  or  $S\mu^2_{\text{CDMS}}$ ) and the experimental  $S\mu^2$  values by Oyama et al. (2023;  $S\mu^2_{\text{SUMIRE}}$ ) are different. Since  $S\mu^2_{\text{SUMIRE}}$  for the  $\text{CH}_2\text{DOH}$  lines that we use is 0.6–0.8 times smaller than  $S\mu^2_{\text{JPL}}$ , its column density derived with is about 1.5 times larger than that with  $S\mu^2_{\text{JPL}}$ . On the other hand, the difference is smaller for  $\text{CHD}_2\text{OH}$ , which does not have a large effect on our column density derivations.

4. With the aid of the infalling-rotating-envelope model FERIA, we find that the  $\text{CH}_3\text{OH}$  ( $18_{3,15} - 18_{2,16}$ , A) emission traces an infalling-rotating envelope with  $M_{\text{star}}$ ,  $r_{\text{CB}} (=R_{\text{in}})$ , and  $i$  are  $0.07M_{\odot}$ , 3 au, and  $70^\circ$ , respectively. Additionally, we study the  $\text{HCOOH}$  ( $12_{0,12} - 11_{0,11}$ ) line with the IRE model and the Keplerian model to examine the existence of the disk structure. The disk structure is not definitively found, and these analyses just suggest a tiny disk structure smaller than 7 au in radius. The low  $M_{\text{star}}$  and the very small disk structure imply a very young protostellar stage of this source.

5. The  $[\text{CH}_2\text{DOH}]/[\text{CH}_3\text{OH}]$  ratio in B335 ([0.09–0.38]) is relatively high among other low-mass protostellar (D/H $\sim$ 0.02) and prestellar sources (D/H $\sim$ 0.034  $\pm$  0.019; van Gelder et al. 2022).  $\text{CH}_2\text{DOH}$  produced on dust grains at the prestellar phase seems to remain in the gas phase after desorption. This result may be related to the youth of the B335 protostar, where fresh gas is being supplied from the outer cold envelope. Further confirmation using optically thin isotopologue lines is necessary.

6. In B335, the  $[\text{CHD}_2\text{OH}]/[\text{CH}_2\text{DOH}]$  ratio ([0.14–0.29]) is higher than the D/H ratio of  $\text{CH}_3\text{OH}$  ( $[\text{CH}_2\text{DOH}]/[\text{CH}_3\text{OH}]/3 = [0.03-0.13]$ ). This feature follows the trend among the other low-mass protostars.

7. The  $[\text{CH}_2\text{DOH}]/[\text{CH}_3\text{OD}]$  ratio in B335 ([4.9–15]) is higher than the statistical weight of 3. This result further supports the systematic trend between low-mass and high-mass sources in previous studies. Even under the high-temperature condition ( $\text{CH}_3\text{OH}$ : 107–217 K and  $\text{CH}_2\text{DOH}$ : 72–188 K) in B335, the  $[\text{CH}_2\text{DOH}]/[\text{CH}_3\text{OD}]$  ratio is still high. This fact means that the ratio would not only depend on the temperature but on current and past physical environments.

### Acknowledgments

This paper makes use of the following ALMA data set: ADS/JAO.ALMA# 2018.1.01311.S (PI: Muneaki Imai). ALMA is a partnership of the ESO (representing its member states), the NSF (USA), and NINS (Japan), together with the NRC (Canada) and the NSC and ASIAA (Taiwan), in cooperation with the Republic of Chile. The Joint ALMA Observatory is operated by the ESO, the AUI/NRAO, and the NAOJ. The authors thank the ALMA staff for their excellent support. This project is supported by a Grant-in-Aid from Japan Society for the Promotion of Science (KAKENHI: Nos.

19H05069, 19K14753, 20H05845, 20H05645 and 22K20390). Y. Okoda thanks RIKEN Special Postdoctoral Researcher Program (Fellowships) for financial support.

### Appendix A Equations for the LTE Calculation

The column densities of  $\text{CH}_3\text{OH}$ ,  $\text{CH}_2\text{DOH}$ ,  $\text{CHD}_2\text{OH}$ , and  $\text{CH}_3\text{OD}$  in the envelope direction are derived under the LTE assumption from the observed intensities and the velocity widths (Table B1). The following formulation is taken from Okoda et al. (2022). Since the dust emission is bright in B335, we explicitly consider the effect of the optical depth of the dust emission ( $\tau_{\text{dust}}$ ) as well as that of the line emission ( $\tau_{\text{line}}$ ). For simplicity, we assume the condition that gas and dust are well mixed and the gas temperature is equal to the dust temperature. In this case, the observed brightness temperature ( $T_{\text{obs}}$ ) is represented as follows:

$$T_{\text{obs}} = \frac{c^2}{2\nu^2 k_{\text{B}}} [B_{\nu}(T) + \exp\{-(\tau_{\text{line}} + \tau_{\text{dust}})\} \{B_{\nu}(T_{\text{cb}}) - B_{\nu}(T)\} - I_{\text{dust}}], \quad (\text{A1})$$

where  $B_{\nu}(T)$  and  $B_{\nu}(T_{\text{cb}})$  are the Planck function for the source temperature at  $T$  and the cosmic microwave background temperature  $T_{\text{cb}}$ , respectively, and  $I_{\text{dust}}$  is the intensity of the dust continuum emission.  $\tau_{\text{line}}$  represents the optical depth of the molecular line, which can be written under the assumption of LTE as:

$$\tau_{\text{line}} = \frac{8\pi^3 S\mu^2}{3h\Delta\nu U(T)} \left\{ \exp\left(\frac{h\nu}{k_{\text{B}}T}\right) - 1 \right\} \exp\left(-\frac{E_u}{k_{\text{B}}T}\right) N, \quad (\text{A2})$$

where  $S$  is the line strength,  $\mu$  the dipole moment responsible for the transition,  $h$  the Planck constant,  $\Delta\nu$  the full width at half maximum,  $U(T)$  the partition function of the molecule at the source temperature  $T$ ,  $\nu$  the frequency,  $E_u$  the upper-state energy, and  $N$  the column density. The  $S\mu^2$  values depend on the transitions (Table 1). We employ the experimental values ( $S\mu^2_{\text{SUMIRE}}$ ) for the lines of  $\text{CH}_2\text{DOH}$  and  $\text{CHD}_2\text{OH}$  in Section 4.1. On the other hand,  $\tau_{\text{dust}}$  is given as:

$$\tau_{\text{dust}} \sim -\ln\left\{\frac{B_{\nu}(T) - I_{\text{dust}}}{B_{\nu}(T)}\right\}, \quad (\text{A3})$$

assuming that  $B_{\nu}(T) \gg B_{\nu}(T_{\text{cb}})$ . The derived  $\tau_{\text{dust}}$  values are summarized in Table C1. Further details are presented by Okoda et al. (2022).

### Appendix B Gaussian Fitting

Using the method described in Appendix A, we perform the analysis on the observed intensities for each molecule at each position. The observed intensities and the velocity widths are obtained by Gaussian fitting. Figure B1 shows examples of the fitting results at the offset of  $-0''.03$ , whose values are summarized in Table B1. In Figure B1, orange lines and black lines represent the fitting and the observation, respectively.

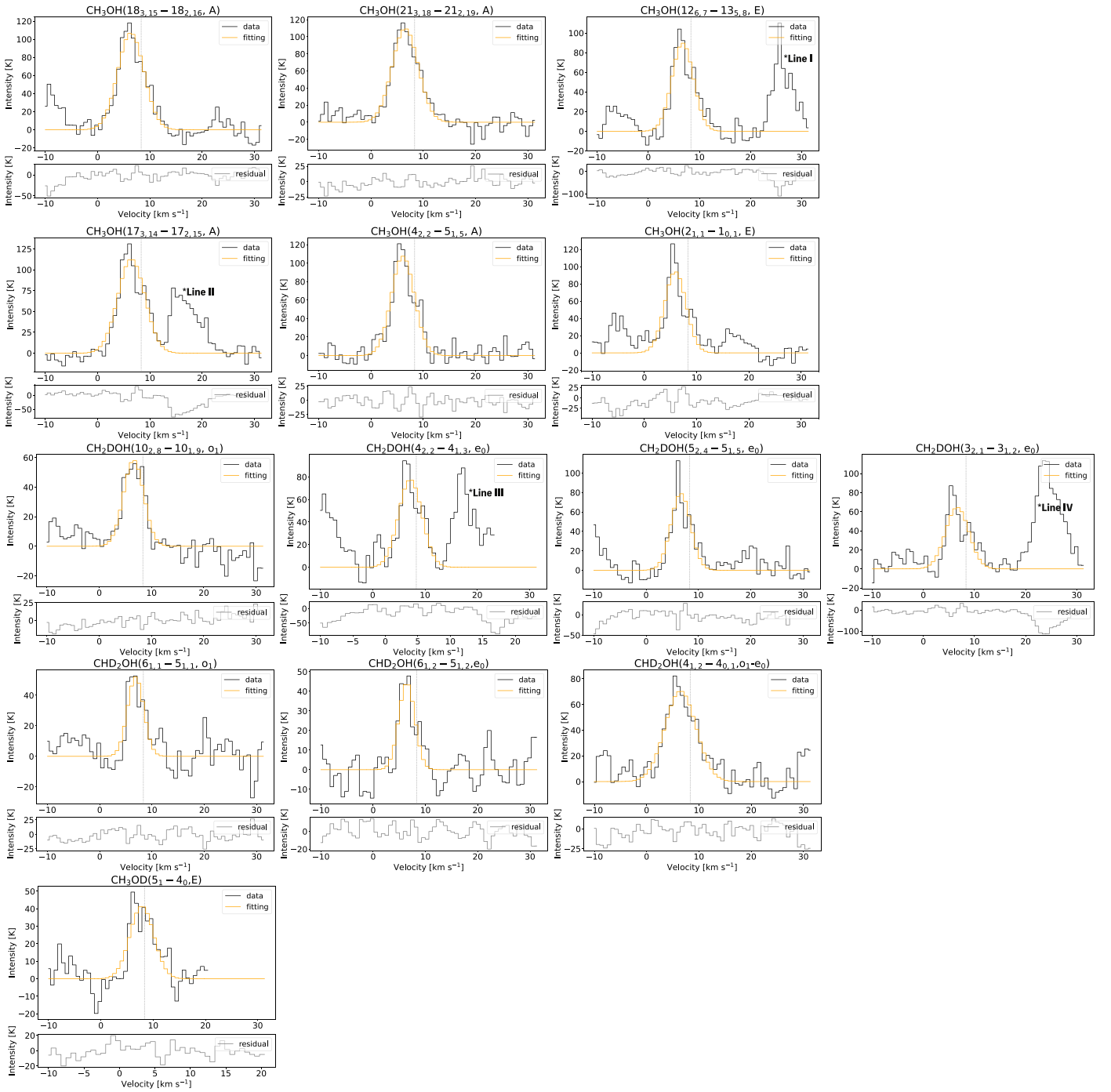


**Figure B1.** Examples of the spectra used for derivation of the column density and the temperature. The spectra are obtained within the rectangle in Figure 1 at the offset of  $-0''.03$ . The Gaussian fitting spectrum in the orange solid line is overlaid with the observed spectrum in black. The systemic velocity is  $8.34 \text{ km s}^{-1}$  (Yen et al. 2015), as shown in gray dotted lines. \*Lines I, II, III and IV are disturbed lines:  $\text{CH}_2\text{DOH}$  ( $5_{2,4} - 5_{1,3}, e_0$ ),  $\text{t-HCOOH}$  ( $11_{3,8} - 10_{3,7}$ ),  $\text{CH}_3\text{CHO}$  ( $13_{0,13} - 12_{0,12}$ , A), and  $\text{CH}_3\text{OH}$  ( $18_{3,15} - 18_{2,16}$ , A), respectively.

**Table B1**  
Examples of the Results of the Gaussian Best-fit Model at the Offset of  $-0''.03$

Line	Transition	Frequency (GHz)	$\delta v$ (km s <sup>-1</sup> ) <sup>a</sup>	$I_{\text{peak}}$ (K) <sup>b</sup>	$V_{\text{sys}}$ (km s <sup>-1</sup> ) <sup>c</sup>
CH <sub>3</sub> OH	18 <sub>3,15</sub> – 18 <sub>2,16</sub> , A	247.610918	5.92 ± 0.33	106.99 ± 5.10	6.36 ± 0.14
CH <sub>3</sub> OH	21 <sub>3,18</sub> – 21 <sub>2,19</sub> , A	245.223019	5.86 ± 0.23	109.73 ± 3.76	6.54 ± 0.10
CH <sub>3</sub> OH	12 <sub>6,7</sub> – 13 <sub>5,8</sub> , E	261.704409	4.96 ± 0.45	89.71 ± 7.05	6.74 ± 0.19
CH <sub>3</sub> OH	17 <sub>3,14</sub> – 17 <sub>2,15</sub> , A	248.282424	6.10 ± 0.76	112.8 ± 12.04	6.46 ± 0.32
CH <sub>3</sub> OH	4 <sub>2,2</sub> – 5 <sub>1,5</sub> , A	247.228587	5.20 ± 0.41	107.49 ± 7.37	6.10 ± 0.17
CH <sub>3</sub> OH	2 <sub>1,1</sub> – 1 <sub>0,1</sub> , E	261.805675	4.84 ± 0.54	94.14 ± 9.15	5.92 ± 0.23
CH <sub>2</sub> DOH	10 <sub>2,8</sub> – 10 <sub>1,9</sub> , o <sub>1</sub>	244.9888456	4.59 ± 0.29	58.33 ± 3.16	6.57 ± 0.12
CH <sub>2</sub> DOH	4 <sub>2,2</sub> – 4 <sub>1,3</sub> , e <sub>0</sub>	244.8411349	5.27 ± 0.60	77.77 ± 7.64	7.18 ± 0.25
CH <sub>2</sub> DOH	5 <sub>2,4</sub> – 5 <sub>1,5</sub> , e <sub>0</sub>	261.6873662	4.45 ± 0.48	79.01 ± 7.38	6.63 ± 0.20
CH <sub>2</sub> DOH	3 <sub>2,1</sub> – 3 <sub>1,2</sub> , e <sub>0</sub>	247.6257463	5.38 ± 0.76	64.61 ± 7.89	6.61 ± 0.32
CHD <sub>2</sub> OH	6 <sub>1,1</sub> – 5 <sub>1,1</sub> , o <sub>1</sub>	246.1432950	3.66 ± 0.52	52.04 ± 6.44	6.87 ± 0.22
CHD <sub>2</sub> OH	6 <sub>1,2</sub> – 5 <sub>1,2</sub> , e <sub>0</sub>	246.2530390	3.59 ± 0.47	44.48 ± 5.07	6.43 ± 0.20
CHD <sub>2</sub> OH	4 <sub>1,2</sub> – 4 <sub>0,1</sub> , o <sub>1</sub> -e <sub>0</sub>	247.2524160	7.01 ± 0.45	70.58 ± 3.82	6.48 ± 0.19
CH <sub>3</sub> OD	5 <sub>1</sub> – 4 <sub>0</sub> , E	245.142988	5.38 ± 0.69	41.6 ± 4.63	7.84 ± 0.29

**Notes.**<sup>a</sup> Line width of the spectrum.<sup>b</sup> Peak intensity of the spectrum.<sup>c</sup> Velocity at the peak intensity of the spectrum.

### Appendix C Dust Optical Depth

Here, we summarize the dust optical depths derived in the analysis in Table C1. They are evaluated by using Equation (A3).

**Table C1**  
Optical Depth and Brightness Temperature of Dust

Position	CH <sub>3</sub> OH	CH <sub>2</sub> DOH	CHD <sub>2</sub> OH	CH <sub>3</sub> OD	$T_{\text{dust}}$ (K) <sup>a</sup>
0.1	0.04 <sup>+0.03</sup> <sub>-0.02</sub>	0.07 <sup>+0.04</sup> <sub>-0.05</sub>	0.04 <sup>+0.03</sup> <sub>-0.02</sub>	0.04 <sup>+0.03</sup> <sub>-0.02</sub>	4.2
0.06	0.12 <sup>+0.02</sup> <sub>-0.02</sub>	0.15 <sup>+0.02</sup> <sub>-0.04</sub>	0.12 <sup>+0.03</sup> <sub>-0.02</sub>	0.12 <sup>+0.03</sup> <sub>-0.02</sub>	15.4
0.03	0.63 <sup>+0.05</sup> <sub>-0.04</sub>	0.78 <sup>+0.04</sup> <sub>-0.05</sub>	0.63 <sup>+0.10</sup> <sub>-0.08</sub>	0.63 <sup>+0.10</sup> <sub>-0.08</sub>	74.0
0	1.01 <sup>+0.10</sup> <sub>-0.03</sub>	1.4 <sup>+0.1</sup> <sub>-0.1</sub>	1.0 <sup>+0.2</sup> <sub>-0.1</sub>	1.0 <sup>+0.2</sup> <sub>-0.1</sub>	136.9
-0.03	0.52 <sup>+0.03</sup> <sub>-0.03</sub>	0.64 <sup>+0.05</sup> <sub>-0.08</sub>	0.52 <sup>+0.07</sup> <sub>-0.06</sub>	0.52 <sup>+0.07</sup> <sub>-0.06</sub>	73.0
-0.06	0.11 <sup>+0.02</sup> <sub>-0.02</sub>	0.12 <sup>+0.03</sup> <sub>-0.03</sub>	0.11 <sup>+0.03</sup> <sub>-0.02</sub>	0.11 <sup>+0.03</sup> <sub>-0.02</sub>	14.7
-0.1	0.04 <sup>+0.02</sup> <sub>-0.03</sub>	0.04 <sup>+0.03</sup> <sub>-0.03</sub>	0.04 <sup>+0.02</sup> <sub>-0.03</sub>	0.04 <sup>+0.02</sup> <sub>-0.03</sub>	4.2

**Notes.**<sup>a</sup> The averaged brightness temperature of dust continuum emission within each rectangle area is shown in Figure 1(a). The noise level of  $T_{\text{dust}}$  (K) is 2.6 K for a rectangle area ( $0''.03 \times 0''.05$ ).

### Appendix D Optical Depths of CH<sub>3</sub>OH Lines

Here, we summarize the optical depths of the CH<sub>3</sub>OH lines derived in the analysis in Table D1. They are evaluated by using Equation (A2).

**Table D1**  
Optical Depths of the CH<sub>3</sub>OH Lines

Position	0''1	0''06	0''03	0''	-0''03	-0''06	-0''1
18 <sub>3,15</sub> – 18 <sub>2,16</sub> , A	12.646	11.566	12.161	6.725	7.382	7.898	8.963
21 <sub>3,18</sub> – 21 <sub>2,19</sub> , A	6.841	6.504	6.814	3.097	4.415	5.099	5.005
12 <sub>6,7</sub> – 13 <sub>5,8</sub> , E	0.783	1.899	2.834	1.739	1.924	1.734	1.061
17 <sub>3,14</sub> – 17 <sub>2,15</sub> , A	3.932	8.621	12.446	6.294	8.898	6.938	5.165
4 <sub>2,2</sub> – 5 <sub>1,5</sub> , A	2.942	7.341	10.819	5.207	7.767	6.176	3.934
2 <sub>1,1</sub> – 1 <sub>0,1</sub> , E	1.162	3.121	5.213	3.377	4.360	2.895	1.576

**Appendix E**  
**D/H ratios in B335 and Other Sources**

The D/H ratios discussed in Section 8.2 are summarized in Table E1. We select the seven low-mass protostellar sources and the low-mass prestellar sources (H-MM1 and L694-2) as samples for comparison. The values of B335 are derived in this paper.

**Table E1**  
Abundances

Source	[CHD <sub>2</sub> OH]/[CH <sub>2</sub> DOH]	[CH <sub>2</sub> DOH]/[CH <sub>3</sub> OH]/3	References <sup>c</sup>
B335	0.14–0.29 <sup>b</sup>	0.03–0.13 <sup>b</sup>	This work
IRAS 16293–2422 A	0.20 ± 0.07	0.028 ± 0.012	1
IRAS 16293–2422 B	0.25 ± 0.09	0.024 ± 0.009	1
B1-c	0.13 ± 0.02	0.028 ± 0.09	2
Serpens S68N	0.12 ± 0.05	0.014 ± 0.006	2
NGC1333 IRAS 2A	0.70 ± 0.26	0.019 ± 0.01	3
NGC1333 IRAS 4A	0.56 ± 0.22	0.014 ± 0.008	3
HOPS373SW	0.75	0.131	4
H-MM1 <sup>a</sup>	0.8 ± 0.4	0.06 ± 0.02	5
L694-2 <sup>a</sup>	0.5 ± 0.3	0.03 ± 0.02	5

**Notes.**<sup>a</sup> Low-mass prestellar core.<sup>b</sup> These values are derived with the experimental value ( $S\mu^2_{\text{SUMIRE}}$ ).<sup>c</sup> 1: Drozdovskaya et al. (2022). 2: van Gelder et al. (2022). 3: Taquet et al. (2019). 4: Lee et al. (2023). 5: Lin et al. (2023).**ORCID iDs**

Yuki Okoda  <https://orcid.org/0000-0003-3655-5270>  
 Nami Sakai  <https://orcid.org/0000-0002-3297-4497>  
 Yoshimasa Watanabe  <https://orcid.org/0000-0002-9668-3592>  
 Ana López-Sepulcre  <https://orcid.org/0000-0002-6729-3640>  
 Takahiro Oyama  <https://orcid.org/0000-0002-2301-7951>  
 Shaoshan Zeng  <https://orcid.org/0000-0003-3721-374X>  
 Satoshi Yamamoto  <https://orcid.org/0000-0002-9865-0970>

**References**

- Ambrose, H. E., Shirley, Y. L., & Scibelli, S. 2021, *MNRAS*, 501, 347  
 Anderson, T., Crownover, R. L., Herbst, E., et al. 1988, *ApJS*, 67, 135  
 Andre, P., Ward-Thompson, D., & Barsony, M. 2000, *Protostars and Planets IV* (Tucson, AZ: Univ. Arizona Press), 59  
 Aso, Y., Ohashi, N., Saigo, K., et al. 2015, *ApJ*, 812, 27  
 Bachiller, R., & Pérez Gutiérrez, M. 1997, *ApJL*, 487, L93  
 Belloche, A., Müller, H. S. P., Garrod, R. T., et al. 2016, *A&A*, 587, A91  
 Bianchi, E., Codella, C., Ceccarelli, C., et al. 2017a, *MNRAS*, 467, 3011  
 Bianchi, E., Codella, C., Ceccarelli, C., et al. 2017b, *A&A*, 606, L7  
 Bizzocchi, L., Caselli, P., Spezzano, S., et al. 2014, *A&A*, 569, A27  
 Bjerkeli, P., Ramsey, J., & Harsono, D. 2023, *A&A*, 677, A62  
 Bjerkeli, P., Ramsey, J. P., Harsono, D., et al. 2019, *A&A*, 631, A64  
 Bøgelund, E. G., McGuire, B. A., Ligterink, N. F. W., et al. 2018, *A&A*, 615, A88  
 Cabedo, V., Maury, A., Girart, J. M., et al. 2021, *A&A*, 653, A166  
 Caselli, P., & Ceccarelli, C. 2012, *A&ARv*, 20, 56  
 Ceccarelli, C., Codella, C., Balucani, N., et al. 2023, *ASP Conf. Ser.* 534, *Protostars and Planets VII* (San Francisco, CA: ASP), 379  
 Charnley, S. B., Tielens, A. G. G. M., & Rodgers, S. D. 1997, *ApJL*, 482, L203  
 Codella, C., Ceccarelli, C., Bianchi, E., et al. 2020, *A&A*, 635, A17  
 Coudert, L. H., Motiyenko, R. A., Margulès, L., et al. 2021, *JMoSp*, 381, 111515  
 Drozdovskaya, M. N., Coudert, L. H., Margulès, L., et al. 2022, *A&A*, 659, A69  
 Drozdovskaya, M. N., Schroeder, I. I. R. H. G., Rubin, M., et al. 2021, *mras*, 500, 4901  
 Duan, Y.-B., Ozier, I., Tsunekawa, S., et al. 2003, *JMoSp*, 218, 95  
 Endres, C. P., Schlemmer, S., Schilke, P., et al. 2016, *JMoSp*, 327, 95  
 Evans, N. J., Di Francesco, J., Lee, J.-E., et al. 2015, *ApJ*, 814, 22  
 Evans, N. J., Yang, Y.-L., Green, J. D., et al. 2023, *ApJ*, 943, 90  
 Faure, A., Faure, M., Theulé, P., et al. 2015, *A&A*, 584, A98  
 Fuchs, G. W., Cuppen, H. M., Ioppolo, S., et al. 2009, *A&A*, 505, 629  
 Garrod, R. T., Wakelam, V., & Herbst, E. 2007, *A&A*, 467, 1103  
 Garrod, R. T., & Widicus Weaver, S. L. 2013, *ChRv*, 113, 8939  
 Geppert, W. D., Hellberg, F., Österdahl, F., et al. 2005, in *IAU Symp.* 231, *Astrochemistry: Recent Successes and Current Challenges*, ed. D. C. Lis et al. (Cambridge: Cambridge Univ. Press), 117  
 Herbst, E., & van Dishoeck, E. F. 2009, *ARA&A*, 47, 427  
 Hidaka, H., Watanabe, M., Kouchi, A., et al. 2009, *ApJ*, 702, 291  
 Hirano, N., Kameya, O., Kasuga, T., et al. 1992, *ApJL*, 390, L85  
 Hirano, N., Kameya, O., Nakayama, M., et al. 1988, *ApJL*, 327, L69  
 Imai, M., Oya, Y., Sakai, N., et al. 2019, *ApJL*, 873, L21  
 Imai, M., Oya, Y., Svoboda, B., et al. 2022, *ApJ*, 934, 70  
 Imai, M., Sakai, N., Oya, Y., et al. 2016, *ApJL*, 830, L37  
 Jacq, T., Walmsley, C. M., Mauersberger, R., et al. 1993, *A&A*, 271, 276

- Jørgensen, J. K., Müller, H. S. P., Calcutt, H., et al. 2018, *A&A*, 620, A170
- Kang, M., Choi, M., Wyrowski, F., et al. 2021, *ApJS*, 255, 2
- Kawanowa, H., Kondo, M., Gotoh, Y., et al. 2004, *SurSci*, 566-568, 1190
- Keene, J., Hildebrand, R. H., Whitcomb, S. E., et al. 1980, *ApJL*, 240, L43
- Kulterer, B. M., Drozdovskaya, M. N., Antonellini, S., et al. 2022, *ESC*, 6, 1171
- Lee, C.-F., Codella, C., Ceccarelli, C., et al. 2022, *ApJ*, 937, 10
- Lee, J.-E., Baek, G., Lee, S., et al. 2023, *ApJ*, 956, 43
- Lin, Y., Spezzano, S., & Caselli, P. 2023, *A&A*, 669, L6
- Manigand, S., Jørgensen, J. K., Calcutt, H., et al. 2020, *A&A*, 635, A48
- McMullin, J. P., Waters, B., Schiebel, D., et al. 2007, *adass XVI*, 127
- Mikami, H., Umemoto, T., Yamamoto, S., et al. 1992, *ApJL*, 392, L87
- Müller, D. R., Altwegg, K., Berthelier, J. J., et al. 2022, *A&A*, 662, A69
- Nagaoka, A., Watanabe, N., & Kouchi, A. 2005, *ApJL*, 624, L29
- Neill, J. L., Crockett, N. R., Bergin, E. A., et al. 2013, *ApJ*, 777, 85
- Ohashi, N., Saigo, K., Aso, Y., et al. 2014, *ApJ*, 796, 131
- Okoda, Y., Oya, Y., Francis, L., et al. 2021, *ApJ*, 910, 11
- Okoda, Y., Oya, Y., Francis, L., et al. 2023, *ApJ*, 948, 127
- Okoda, Y., Oya, Y., Imai, M., et al. 2022, *ApJ*, 935, 136
- Okoda, Y., Oya, Y., Sakai, N., et al. 2018, *ApJL*, 864, L25
- Osamura, Y., Roberts, H., & Herbst, E. 2004, *A&A*, 421, 1101
- Oya, Y. 2020, IAU SYmp. 345, *Origins: From the Protosun to the First Steps of Life* (Cambridge: Cambridge Univ. Press), 111
- Oya, Y., Kibukawa, H., Miyake, S., et al. 2022, *PASP*, 134, 094301
- Oya, Y., Sakai, N., López-Sepulcre, A., et al. 2016, *ApJ*, 824, 88
- Oya, Y., & Yamamoto, S. 2020, *ApJ*, 904, 185
- Oyama, T., Ohno, Y., Tamanai, A., et al. 2023, *ApJ*, 957, 4
- Parise, B., Castets, A., Herbst, E., et al. 2004, *A&A*, 416, 159
- Parise, B., Ceccarelli, C., Tielens, A. G. G. M., et al. 2006, *A&A*, 453, 949
- Peng, T.-C., Despois, D., Brouillet, N., et al. 2012, *A&A*, 543, A152
- Pickett, H. M., Poynter, R. L., Cohen, E. A., et al. 1998, *JQSRT*, 60, 883
- Ratajczak, A., Quirico, E., Faure, A., et al. 2009, *A&A*, 496, L21
- Ratajczak, A., Taquet, V., Kahane, C., et al. 2011, *A&A*, 528, L13
- Rodgers, S. D., & Charnley, S. B. 2002, *P&SS*, 50, 1125
- Souda, R., Kawanowa, H., Kondo, M., et al. 2003, *JChPh*, 119, 6194
- Stutz, A. M., Rubin, M., Werner, M. W., et al. 2008, *ApJ*, 687, 389
- Taquet, V., Bianchi, E., Codella, C., et al. 2019, *A&A*, 632, A19
- Taquet, V., Ceccarelli, C., & Kahane, C. 2012, *A&A*, 538, A42
- Taquet, V., Charnley, S. B., & Sipilä, O. 2014, *ApJ*, 791, 1
- Taquet, V., Peters, P. S., Kahane, C., et al. 2013, *A&A*, 550, A127
- van Gelder, M. L., Jaspers, J., Nazari, P., et al. 2022, *A&A*, 667, A136
- van Gelder, M. L., Tabone, B., Tychoniec, L., et al. 2020, *A&A*, 639, A87
- Vastel, C., Alves, F., Ceccarelli, C., et al. 2022, *A&A*, 664, A171
- Watanabe, N., & Kouchi, A. 2002, *ApJL*, 571, L173
- Watson, D. M. 2020, *RNAAS*, 4, 88
- Wilkins, O. H., & Blake, G. A. 2022, *JPCA*, 126, 6473
- Yamamoto, S. 2017, *Introduction to Astrochemistry: Chemical Evolution from Interstellar Clouds to Star and Planet Formation* (Berlin: Springer)
- Yamato, Y., Notsu, S., Aikawa, Y., et al. 2024, *AJ*, 167, 66
- Yen, H.-W., Takakuwa, S., Koch, P. M., et al. 2015, *ApJ*, 812, 129